

Numerical aspects of eigenvalue and eigenfunction computations for chaotic quantum systems

Arnd Bäcker¹

Abteilung Theoretische Physik
 Universität Ulm, Albert-Einstein-Allee 11
 D-89081 Ulm, Germany

Abstract:

We give an introduction to some of the numerical aspects in quantum chaos. The classical dynamics of two-dimensional area-preserving maps on the torus is illustrated using the standard map and a perturbed cat map. The quantization of area-preserving maps given by their generating function is discussed and for the computation of the eigenvalues a computer program in Python is presented. We illustrate the eigenvalue distribution for two types of perturbed cat maps, one leading to COE and the other to CUE statistics. For the eigenfunctions of quantum maps we study the distribution of the eigenvectors and compare them with the corresponding random matrix distributions. The Husimi representation allows for a direct comparison of the localization of the eigenstates in phase space with the corresponding classical structures. Examples for a perturbed cat map and the standard map with different parameters are shown.

Billiard systems and the corresponding quantum billiards are another important class of systems (which are also relevant to applications, for example in mesoscopic physics). We provide a detailed exposition of the boundary integral method, which is one important method to determine the eigenvalues and eigenfunctions of the Helmholtz equation. We discuss several methods to determine the eigenvalues from the Fredholm equation and illustrate them for the stadium billiard. The occurrence of spurious solutions is discussed in detail and illustrated for the circular billiard, the stadium billiard, and the annular sector billiard.

We emphasize the role of the normal derivative function to compute the normalization of eigenfunctions, momentum representations or autocorrelation functions in a very efficient and direct way. Some examples for these quantities are given and discussed.

¹E-mail address: arnd.baecker@physik.uni-ulm.de, homepage: www.uni-ulm.de/theo/qc/baec.

1 Introduction

In this text, which is an expanded version of lectures held at a summer school in Bologna in 2001, we give an introduction to some of the numerical aspects in quantum chaos; some of the sections on the boundary integral method contain more advanced material. In quantum chaos one studies quantum systems whose classical limit is (in some sense) chaotic. In this subject computer experiments play an important role. For integrable systems the eigenvalues and eigenfunctions can be determined either explicitly or as solutions of simple equations. In contrast, for chaotic systems there are no explicit formulae for eigenvalues and eigenfunctions such that numerical methods have to be used. In many cases numerical observations have lead to the formulation of important conjectures. Such numerical computations also allow us to test analytical results which have been derived under certain assumptions or by using approximations.

An important class of systems for the study of classical chaos are area-preserving maps as several types of different dynamical behaviour like integrable motion, mixed dynamics, ergodicity, mixing or Anosov systems can be found. We discuss the numerics for the corresponding quantum maps and illustrate some of the methods and results using the standard map and the perturbed cat map as prominent examples.

Another important class of systems are classical billiards and the corresponding quantum billiards. In section 3 we discuss in detail the boundary integral method, which is one of the main methods for the solution of the Helmholtz equation, which is the time-independent Schrödinger equation for these systems.

2 Area preserving maps

2.1 Some examples

We will restrict ourselves to area-preserving maps on the two-torus

$$P : \mathbb{T}^2 \rightarrow \mathbb{T}^2 \tag{1}$$

$$(q, p) \mapsto (q', p') , \tag{2}$$

where $\mathbb{T}^2 \simeq \mathbb{R}^2/\mathbb{Z}^2$, i.e. the map is defined on a square with opposite sides identified. The requirement that the map P is area-preserving is equivalent to the condition that $\det DP = 1$, where DP is the linearization of the map P . The natural invariant measure on \mathbb{T}^2 is the Lebesgue measure $d\mu = dqdp$.

As a first example let us consider the so-called *standard map*, defined by

$$\begin{pmatrix} q' \\ p' \end{pmatrix} = \begin{pmatrix} q + p - \frac{\kappa}{2\pi} \sin(2\pi q) \\ p - \frac{\kappa}{2\pi} \sin(2\pi q) \end{pmatrix} \mod 1 . \tag{3}$$

One easily checks that this map is area-preserving. Fig. 1 shows some orbits (i.e. for different initial points (q, p) the points $(q_n, p_n) = P^n(q, p)$ are plotted for $n \leq 1000$) of the standard map for different parameters κ . For $\kappa = 0$ an initial point (q, p) stays on the horizontal line and in q it rotates with frequency p . So for irrational p the corresponding line is filled densely. For $\kappa > 0$, the lines with rational p break up into an island-chain structure composed of (initially) stable orbits and their corresponding unstable (hyperbolic) partner. For small enough perturbation there are invariant (Kolmogorov–Arnold–Moser or short KAM) curves which are absolute barriers to the

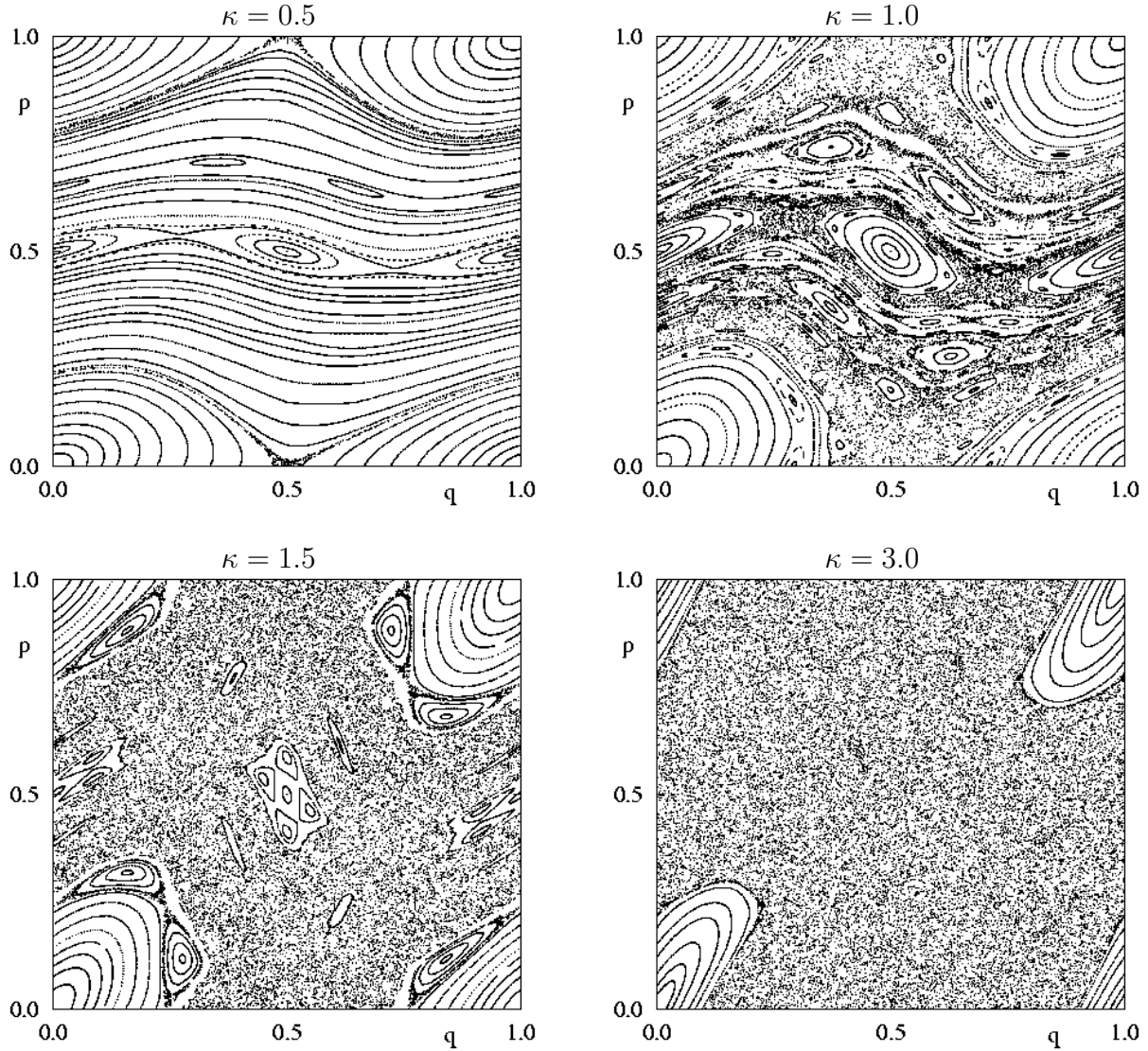


Figure 1: Examples of orbits in the standard map for different parameters κ .

motion (for a more detailed discussion of these aspects the review [1] is a good starting point). For stronger perturbations, e.g. $\kappa = 1$ or $\kappa = 1.5$, the stochastic bands become larger and for even stronger perturbation (see the picture for $\kappa = 3.0$) there appears to be just one quite big stochastic region together with the elliptic island. The elliptic islands coexist with regions of irregular motion, therefore the standard map is an example of a so-called system with mixed phase space or, more briefly, a *mixed system*. Whether the motion in those stochastic regions is ergodic is one of the big unsolved problems, see [2] for a review on the coexistence problem. For some recent results on the classical dynamics of the standard map, in particular at large parameters, see [3–5].

An alternative way to specify a map $P : \mathbb{T}^2 \rightarrow \mathbb{T}^2$ is to use a generating function $S(q', q)$, from which the map is obtained by

$$p = -\frac{\partial S(q', q)}{\partial q} \quad p' = \frac{\partial S(q', q)}{\partial q'} . \quad (4)$$

One easily checks that

$$S(q', q) = \frac{1}{2}(q - q')^2 + \frac{\kappa}{4\pi^2} \cos(2\pi q) , \quad (5)$$

is a generating function for the standard map (3).

Another important class are perturbed cat maps [6, 7], like

$$\begin{pmatrix} q' \\ p' \end{pmatrix} = A \begin{pmatrix} q \\ p \end{pmatrix} + \kappa G(q) \begin{pmatrix} A_{12} \\ A_{22} \end{pmatrix} \quad \text{mod 1} , \quad (6)$$

where

$$A = \begin{pmatrix} A_{11} & A_{12} \\ A_{21} & A_{22} \end{pmatrix} \quad (7)$$

is a matrix with integer entries (ensuring the continuity of the map), $\det A = 1$ (area preservation) and $\text{Tr } A > 2$ (hyperbolicity). The perturbation $G(q)$ is a smooth periodic function on $[0, 1]$. For $\kappa = 0$ the mapping is Anosov (see e.g. [8]), in particular it is ergodic and mixing. Moreover, following from the the Anosov theorem the map (6) is structurally stable, i.e. it stays Anosov as long

$$\kappa \leq \kappa_{\max} := \frac{\sqrt{(\text{Tr } A)^2 - 4} - \text{Tr } A + 2}{2 \max_q |G'(q)| \sqrt{1 + A_{22}^2}} ; \quad (8)$$

in particular the orbits are topologically conjugate to those of the unperturbed cat map. For larger parameters there are typically elliptic islands, so it becomes a mixed system.

A common choice for A and the perturbation is

$$\begin{pmatrix} q' \\ p' \end{pmatrix} = \begin{pmatrix} 2 & 1 \\ 3 & 2 \end{pmatrix} \begin{pmatrix} q \\ p \end{pmatrix} + \frac{\kappa}{2\pi} \cos(2\pi q) \begin{pmatrix} 1 \\ 2 \end{pmatrix} \quad \text{mod 1} . \quad (9)$$

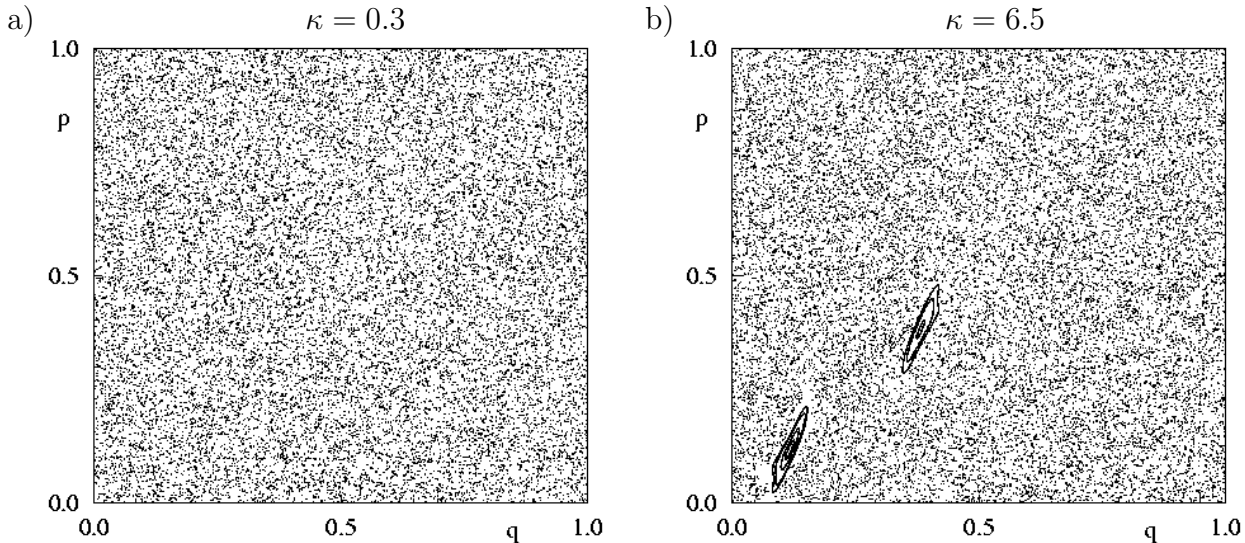


Figure 2: Examples of orbits in the perturbed cat map (9) for $\kappa = 0.3$ and $\kappa = 6.5$.

For $\kappa \leq \kappa_{\max} = (\sqrt{3} - 1)/\sqrt{5} = 0.33\dots$ the map is Anosov. The corresponding generating function is given by

$$S(q', q) = q'^2 - qq' + q^2 + \frac{\kappa}{4\pi^2} \sin(2\pi q) . \quad (10)$$

In fig. 2a) one orbit for 20 000 iterations for the perturbed cat map (9) with $\kappa = 0.3$ is shown. The orbit appears to fill the torus in a uniform way, as it has to be asymptotically for almost all initial conditions because of the ergodicity of the map. For $\kappa = 6.5$ fig. 2b) shows one orbit (20 000 iterates) in the irregular component and some orbits (1000 iterations) in the elliptic islands.

2.2 Quantization of area-preserving maps

For the quantization of area-preserving maps exist several approaches, see for example [9–13, 6, 14–16]; a detailed account can be found in [17], and [18] provides a pedagogical introduction to the subject. First one has to find a suitable Hilbert space which incorporates the topology of the torus \mathbb{T}^2 , i.e. the eigenfunctions in position and momentum have to fulfil

$$\psi(q + j) = e^{\frac{i}{\hbar}j\theta_2}\psi(q) \quad ; \quad j \in \mathbb{N} \quad (11)$$

$$\widehat{\psi}(p + k) = e^{-\frac{i}{\hbar}k\theta_1}\widehat{\psi}(p) \quad ; \quad k \in \mathbb{N} . \quad (12)$$

These conditions imply that Planck's constant \hbar can only take the values $\hbar = \frac{1}{2\pi N}$ with $N \in \mathbb{N}$. Thus the semiclassical limit $\hbar \rightarrow 0$ corresponds to $N \rightarrow \infty$. The phases $(\theta_1, \theta_2) \in [0, 1]^2$ are at first arbitrary; for $\theta_1 = \theta_2 = 0$ one obtains periodic boundary conditions. For each N one has a Hilbert space \mathcal{H}_N of finite dimension N . Observables $f \in C^\infty(\mathbb{T}^2)$ can be quantized analogous to the Weyl quantization to give an operator $\text{Op}(f)$ on \mathcal{H}_N . Finally, a quantum map is a sequence of unitary operators U_N , $N \in \mathbb{N}$ on a Hilbert space \mathcal{H}_N . The quantum map is a quantization of a classical map P on \mathbb{T}^2 , if the so-called Egorov property is fulfilled, i.e.

$$\lim_{N \rightarrow \infty} \|U_N^{-1}\text{Op}(f)U_N - \text{Op}(f \circ P)\| = 0 \quad \forall f \in C^\infty(\mathbb{T}^2) . \quad (13)$$

This means that semiclassically quantum time evolution and classical time evolution commute.

So the aim is to find for a given classical map a corresponding sequence of unitary operators. Unfortunately, this is not as straight forward as the quantization of Hamiltonian systems and a lot of information on this can be found in the above cited literature and references therein. One of the simplest approaches to determine U_N corresponding to a given area-preserving map uses its generating function to define

$$(U_N)_{j',j} := \langle q_{j'} | U_N | q_j \rangle = \frac{1}{\sqrt{N}} \left| \frac{\partial^2 S(\tilde{q}', \tilde{q})}{\partial \tilde{q}' \partial \tilde{q}} \right|_{\tilde{q}'=q_{j'}, \tilde{q}=q_j}^{1/2} \exp(2\pi i N S(q_{j'}, q_j)) \quad (14)$$

with $q_j = j/N$, $q_{j'} = j'/N$, where $j, j' = 0, 1, \dots, N-1$. In the same way one may (and for certain maps which cannot be represented in terms of $S(q', q)$ one has to) use other generating functions such as $S(p', p)$ or $S(q, p)$; usually these will lead to different eigenvalues and eigenfunctions. The question is to determine conditions on the generating function $S(q', q)$ such that U_N is unitary and fulfills the Egorov property (13). To my knowledge this question has not yet been fully explored, even though the quantum maps studied in the literature provide both examples and counterexamples. We will leave this as an interesting open question.

For the examples introduced before the quantization via (14) can be used. For the standard map we get

$$(U_N)_{j',j} = \frac{1}{\sqrt{N}} \exp \left[\frac{i\pi}{N} (j' - j)^2 + \frac{i\kappa N}{2\pi} \cos \left(\frac{2\pi}{N} j \right) \right] \quad (15)$$

with $j, j' = 0, \dots, N - 1$. A quantization of the standard map which takes the symmetries into account can be found in [19]. For the perturbed cat map (9) one gets using its generating function (10)

$$(U_N)_{j',j} = \frac{1}{\sqrt{N}} \exp \left(\frac{2\pi i}{N} (j'^2 - j'j + j^2 + \kappa/(4\pi^2) \sin(2\pi j/N)) \right) . \quad (16)$$

For the unitary operator one has to solve the eigenvalue problem

$$U_N \psi_n = \lambda_n \psi_n \quad \text{with } n = 0, \dots, N - 1, \quad \psi_n \in \mathbb{C}^N . \quad (17)$$

Here λ_n is the n -th eigenvalue and the corresponding eigenvector ψ_n consists of N complex components, where N is the size of the unitary matrix U_N . Because of the unitarity of U_N the eigenvalues lie on the unit circle, i.e. $|\lambda_n| = 1$.

Let us discuss some of the numerical aspects relevant for finding the solutions of (17) without going into implementation specific details (see the appendix and [20] for an implementation using Python).

Computing the eigenvalues of (17) consists of two main steps

- Setting up the matrix U_N :

The computational effort increases proportional to N^2 (unless each matrix element requires further loops) as we have to fill the N^2 matrix elements.

The memory requirement to store U_N is $16 N^2$ Bytes (for a IEEE-compliant machine a double precision floating point number requires 8 Bytes; as we have both real and imaginary part we end up with 16 Bytes per matrix element).

- Computing the eigenvalues:

The computational effort for the matrix diagonalization (typically) scales like N^3 .

Usually one will use a black-box routine such as one from the NAG-library [21] or from LAPACK [22]. To my knowledge there are no routines which make use of the fact that the matrix U_N is unitary so we may for example use the NAG routine F02GBF or the LAPACK routine ZGEEES (or the more recent routine ZGEEV which is faster for larger matrices, e.g. $N \geq 500$) which compute all eigenvalues of a complex matrix.

For certain maps specific optimizations are possible, see e.g. [19] for the standard map. For this type of mapping a different approach employing a combination of fast Fourier transform and Lanczos method reduces the computational effort to $N^2 \ln N$ [23].

After successful compilation and running of the program it is useful to see whether the eigenvalues really lie on the unit circle. In fig. 3 this is illustrated for $N = 200$ and the standard map with $\kappa = 1.5$. For small N the running times of the program for setting up the matrix U_N and its diagonalization is just a matter of minutes. For example on an Intel Pentium III processor with 666 MHz one needs just 6 minutes to compute the eigenvalues of (17) when $N = 1000$. However,

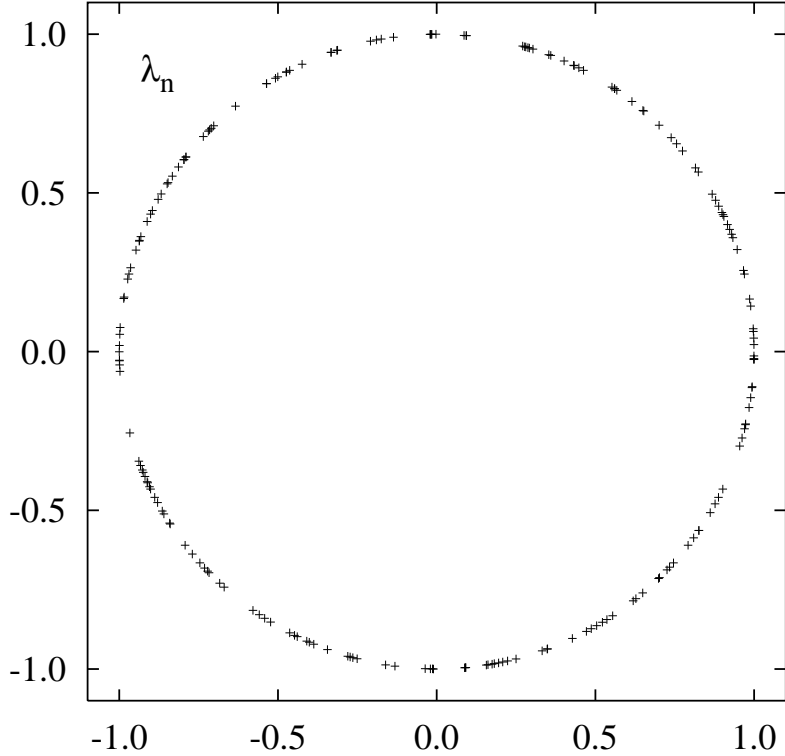


Figure 3: Plotting the eigenvalues of U_N allows to check the numerical implementation and the unitarity of U_N ; the picture shows for $N = 200$ and $\kappa = 1.5$ the eigenvalues λ_n for the quantized standard map (15).

for $N = 3000$ already 140 MB of RAM are required to store U_N and the computing time increases to 6 hours. Depending on available memory, computing power, patience and motivation one may use larger values of N .

Let us conclude this part with a more technical remark: In addition to the choice of computer language, compiler, optimizations and algorithm there is one very important component for achieving good performance when doing numerical linear algebra computations: the BLAS (Basic Linear Algebra Subprograms). Libraries such as LAPACK defer all the basics tasks like adding vectors, vector-matrix or matrix-matrix multiplication to the BLAS such that highly optimized (machine-specific) BLAS routines should be used. Most hardware vendors provide these (of differing quality). Recently the software system ATLAS (Automatically Tuned Linear Algebra Software) [24] has been introduced which generates a machine dependent optimized BLAS library. For some computers ATLAS-based BLAS can be even faster than the vendor supplied ones!

2.3 Eigenvalue statistics

One central research line in quantum chaos is the investigation of spectral statistics. It has been conjectured [25] that for generic chaotic systems the eigenvalue statistics can be described by

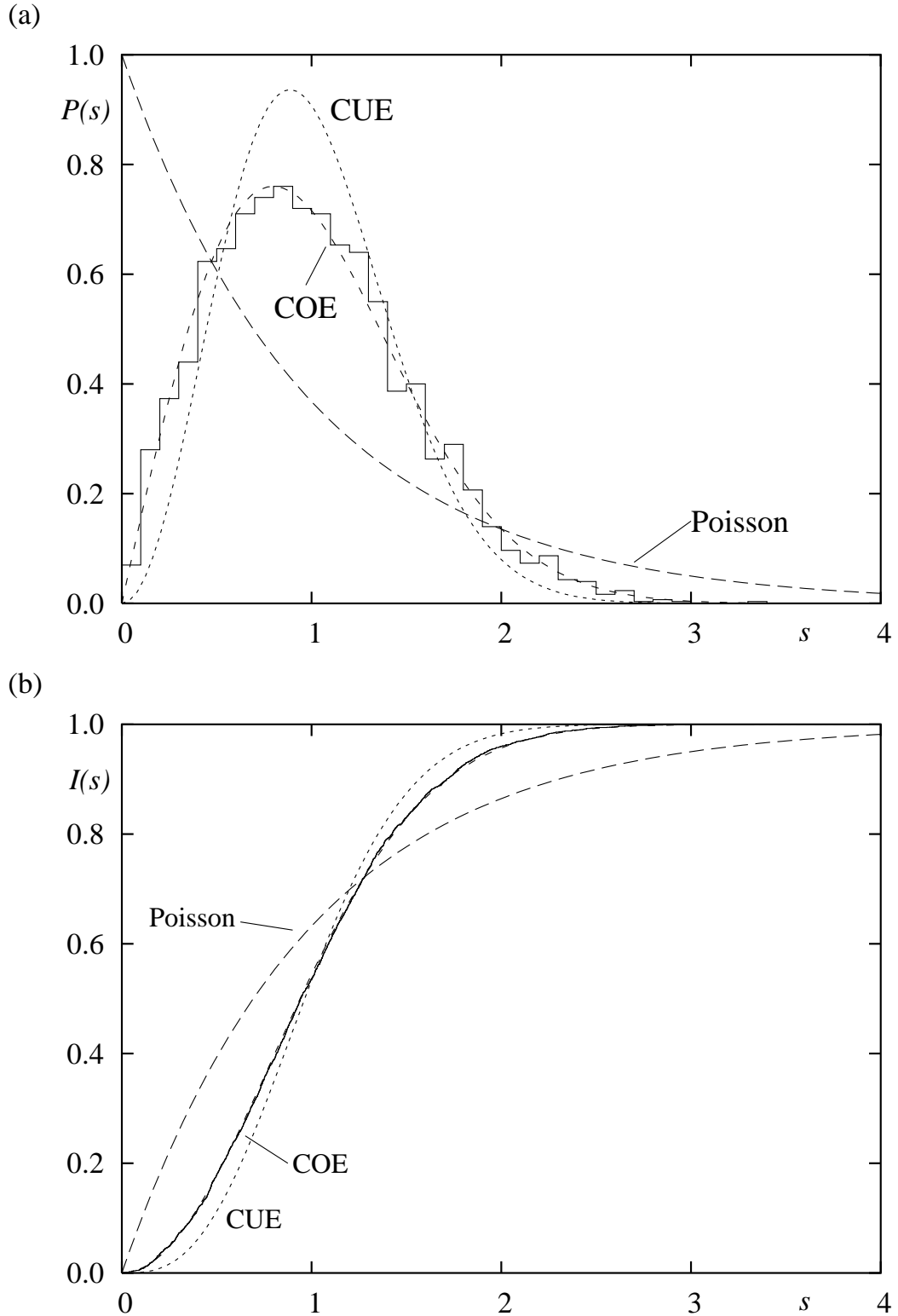


Figure 4: (a) Level spacing distribution $P(s)$ and (b) cumulative level spacing distribution $I(s)$ for the perturbed cat map (9) with $\kappa = 0.3$ and $N = 3001$.

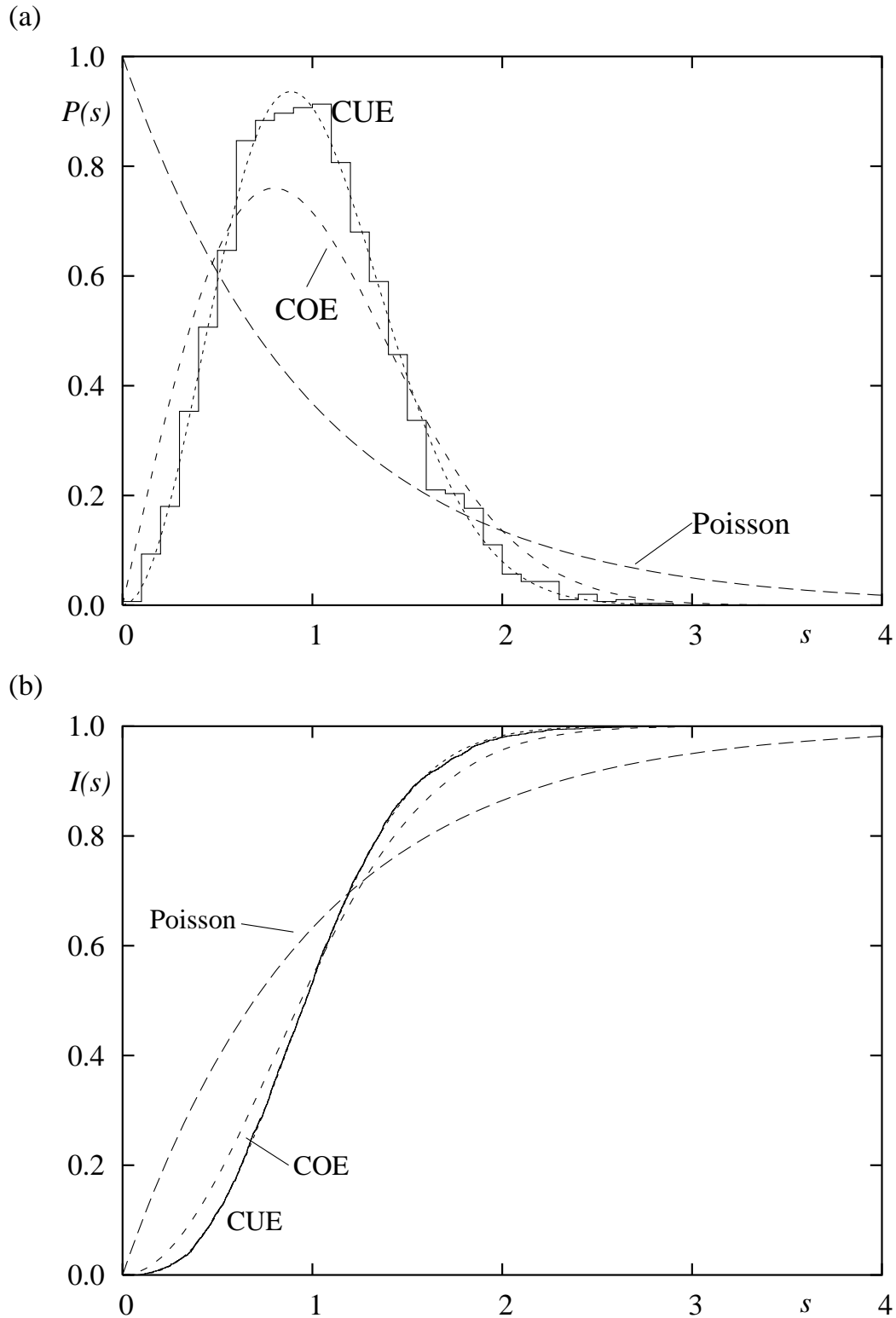


Figure 5: (a) Level spacing distribution $P(s)$ and (b) cumulative level spacing distribution $I(s)$ for the perturbed cat map (22) with $\kappa_p = \kappa_q = 0.012$ and $N = 3001$.

random matrix theory, whereas generic integrable systems should follow Poissonian statistics [26]. To study the eigenvalue statistics for quantum maps one considers the eigenphases $\varphi_n \in [0, 2\pi[$, defined by $\lambda_n = e^{i\varphi_n}$ (in the following we will also call φ_n levels in analogy to the energy levels for the Schrödinger equation). The simplest statistics is the nearest neighbour level spacing distribution $P(s)$ which is the distribution of the spacings

$$s_n := \frac{N}{2\pi}(\varphi_{n+1} - \varphi_n) \quad \text{with } n = 0, \dots, N-1 \quad \text{and } \varphi_N := \varphi_0 .$$

The factor $\frac{N}{2\pi}$ ensures that the average of all spacings s_n is 1. To compute the distribution practically one chooses a division of the interval $[0, 10]$ (usually this interval is sufficient, but more precisely the upper limit is determined by the largest s_n) into b bins and determines the fraction of spacings s_n falling into the corresponding bins. If N is too small it is better to consider instead of $P(s)$ the corresponding cumulative distribution

$$I(s) := \frac{\#\{n \mid s_n \leq s\}}{N} \quad (18)$$

which avoids the binning and results in a smoother curve.

Fig. 4 shows for the perturbed cat map (9) with $\kappa = 0.3$ the level spacing distribution $P(s)$ and the cumulative level spacing distribution $I(s)$ for $N = 3001$. For this parameter value κ the map is still Anosov so one expects that the correlations of the eigenphases follow random matrix theory; in particular because the perturbation should break up the number theoretical degeneracies which lead to non-generic spectral statistics for the cat maps at $\kappa = 0$ [27, 28]. In [29, 30] it is shown that for all perturbations which are just a shear in position one of the symmetries of the cat map survives, so that the statistics are expected to be described by the circular orthogonal ensemble (COE). In the limit $N \rightarrow \infty$ this is the same as the Gaussian orthogonal ensemble (GOE). In fig. 4 we show the Wigner distribution $P_{\text{Wigner}}(s)$ which is very close to the COE distribution,

$$P_{\text{COE}}(s) \approx P_{\text{Wigner}}(s) = \frac{\pi}{2}s \exp\left(-\frac{\pi}{4}s^2\right) . \quad (19)$$

and for comparison the CUE distribution

$$P_{\text{CUE}}(s) \approx \frac{32}{\pi^2}s^2 \exp\left(-\frac{4}{\pi}s^2\right) \quad (20)$$

and the Poisson distribution (expected for generic integrable systems)

$$P_{\text{Poisson}}(s) = e^{-s} . \quad (21)$$

The agreement with the expected COE distribution is very good.

A specific example, which breaks the above mentioned unitary symmetry and thus leads to CUE statistics, uses two shears, one in position and one in momentum [29],

$$\begin{pmatrix} q' \\ p' \end{pmatrix} = (A \circ P_q \circ P_p) \begin{pmatrix} q \\ p \end{pmatrix} , \quad (22)$$

where

$$A = \begin{pmatrix} 12 & 7 \\ 41 & 24 \end{pmatrix} \quad (23)$$

and $P_q(q, p) = (q + \kappa_q G(p), p)$, $P_p(q, p) = (q, p + \kappa_p F(q))$ with $F(q) = \frac{1}{2\pi}(\sin(2\pi q) - \sin(4\pi q))$ and $G(p) = \frac{1}{2\pi}(\sin(4\pi p) - \sin(2\pi p))$. For the corresponding quantum map with $\kappa_p = \kappa_q = 0.012$ and $N = 3001$ the level spacing distribution is shown in fig. 5. One observes very good agreement with the CUE distribution.

2.4 Eigenfunctions

Another interesting question concerns the statistical behaviour of eigenfunctions, and more specifically for quantum maps the eigenvector statistics and the properties of phase space representations like the Husimi function.

2.4.1 Eigenvector distributions

Consider an eigenvector ψ of a quantum map given by the N numbers $c_j \in \mathbb{C}$, $j = 0, \dots, N-1$. The distribution $P(\psi)$ is given (similarly to the level spacing distribution) by

$$\frac{1}{N} \# \{a \leq |c_j|^2 \leq b\} = \int_a^b P(\psi) d\psi . \quad (24)$$

Let us first discuss the corresponding random matrix results (see e.g. [31, 32]). For the COE the eigenvectors can be chosen to be real and the coefficients c_j , $j = 0, \dots, N-1$, only have to obey the normalization condition

$$\sum_{j=0}^{N-1} c_j^2 = 1 \quad \text{with } c_j \in \mathbb{R} . \quad (25)$$

Thus the joint probability for an eigenvector $\mathbf{c} = (c_0, \dots, c_{N-1}) \in \mathbb{R}^N$ is

$$P_N^{\text{COE}}(\mathbf{c}) = \frac{\Gamma(N/2)}{\pi^{N/2}} \delta \left(1 - \sum_{j=0}^{N-1} c_j^2 \right) , \quad (26)$$

where the prefactor ensures normalization. So the probability of one component to have a specific value y is given by integrating $P_N^{\text{COE}}(\mathbf{c})$ over all other components,

$$P_N^{\text{COE}}(y) = \int \delta(y - c_1^2) P_N^{\text{COE}}(\mathbf{c}) dc_0 \cdots dc_{N-1} = \frac{1}{\sqrt{\pi y}} \frac{\Gamma(N/2)}{\Gamma((N-1)/2)} (1-y)^{(N-3)/2} . \quad (27)$$

The mean of $P_N^{\text{COE}}(y)$ is $\int_0^1 y P_N^{\text{COE}}(y) dy = 1/N$. So using the rescaling $\eta = yN$ gives

$$P_N^{\text{COE}}(\eta) = \frac{1}{\sqrt{\pi N \eta}} \frac{\Gamma(N/2)}{\Gamma((N-1)/2)} (1-\eta/N)^{(N-3)/2} . \quad (28)$$

In the limit of large N one gets the so-called Porter-Thomas distribution [33]

$$P_N^{\text{COE}}(\eta) = \frac{1}{\sqrt{2\pi\eta}} \exp(-\eta/2) , \quad (29)$$

and the corresponding cumulative distribution $I(y) = \int_0^y P(y') dy'$ reads

$$I(\eta) = \text{erf} \left(\sqrt{\eta/2} \right) . \quad (30)$$

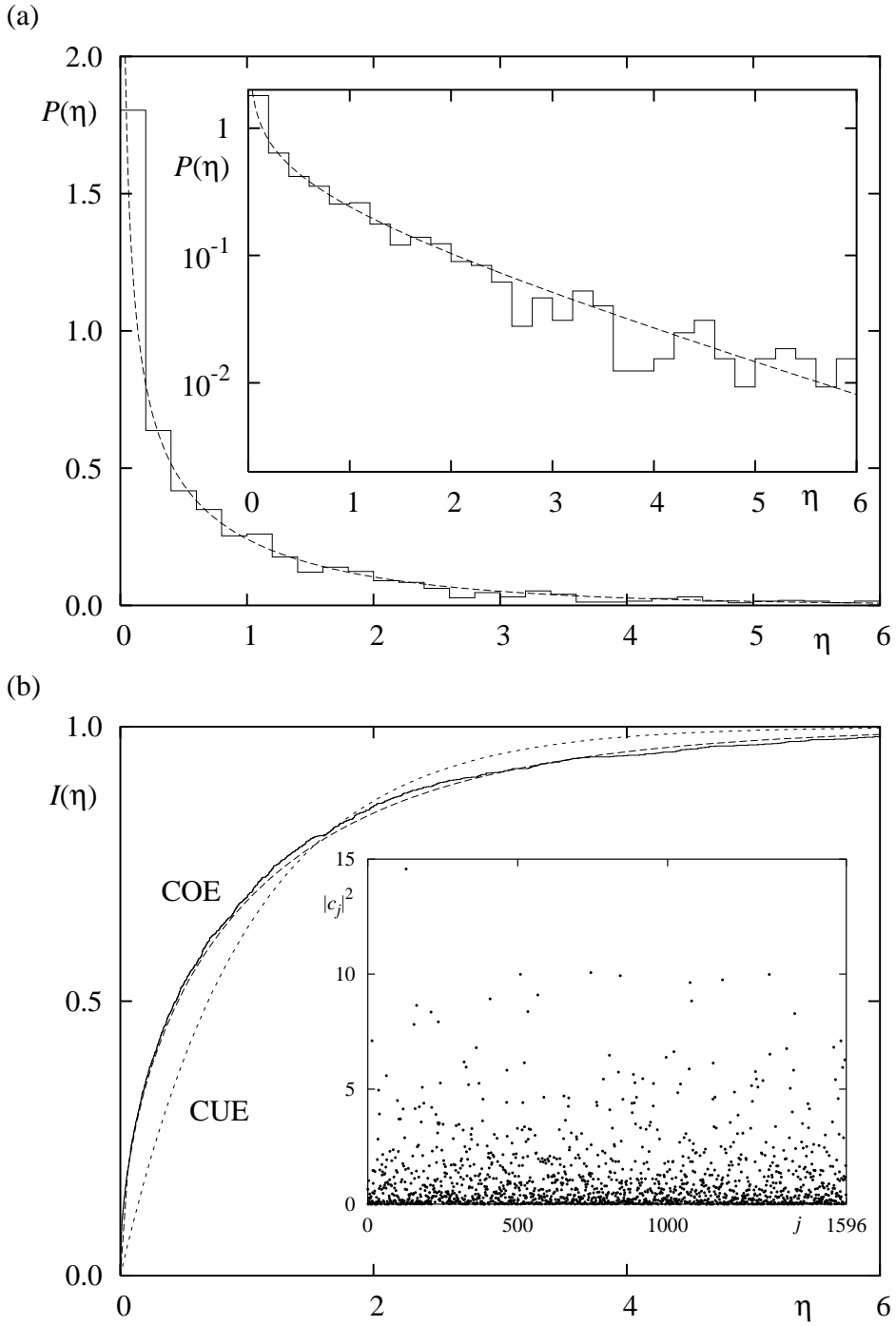


Figure 6: (a) Eigenvector distribution for the perturbed cat map (9) with $N = 1597$ and $\kappa = 0.3$. In comparison with the asymptotic COE distribution, eq. (28), dashed line. The inset shows the same curves in a log–normal plot. In (b) the cumulative distribution is shown and in the inset a plot of the absolute value of the components $c_j^{(n)}$, $j = 0, \dots, N - 1$ of the corresponding eigenvector $\psi_{n=20}$ is displayed.

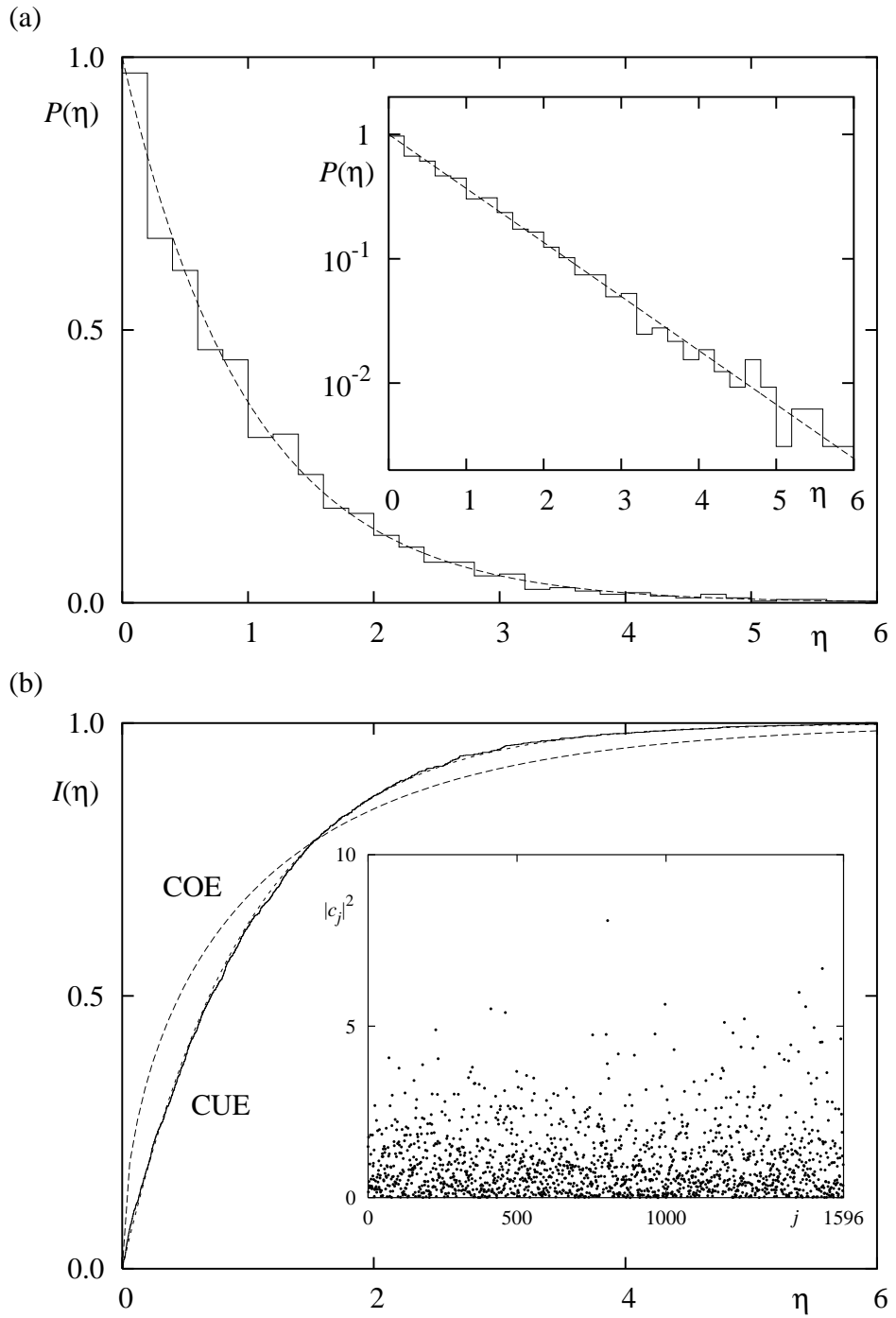


Figure 7: (a) Eigenvector distribution of an eigenvector for the perturbed cat map (22) with $N = 1597$ and $\kappa_p = \kappa_q = 0.012$ is shown in comparison with the asymptotic CUE distribution, eq. (35), dashed line. The inset shows the same curves in a log-normal plot. In (b) the corresponding cumulative distributions are shown and in the inset a plot of the absolute value of the components $c_j^{(n)}$, $j = 0, \dots, N - 1$ of the corresponding eigenvector $\psi_{n=2}$ is displayed.

Fig. 6 shows an example for the eigenvector distribution of an eigenstate of the perturbed cat map (9) with $\kappa = 0.3$ and $N = 1597$. There is good agreement with the expected COE distribution, eq. (29), shown as dashed line.

Finally, let us consider again the map (22) which shows CUE level statistics. From this one would expect that also the eigenvector statistics follows the CUE. Similar to the case of the COE one has the normalization condition

$$\sum_{j=0}^{N-1} |c_j|^2 = 1 \quad \text{with } c_j \in \mathbb{C} \quad . \quad (31)$$

Thus the joint probability for an eigenvector $\mathbf{c} = (c_0, \dots, c_{N-1}) \in \mathbb{C}^N$ reads

$$P_N^{\text{CUE}}(\mathbf{c}) = \frac{\Gamma(N)}{\pi^N} \delta \left(1 - \sum_{j=0}^{N-1} |c_j|^2 \right) \quad . \quad (32)$$

The probability of one component to have a specific value y is given by integrating $P_N^{\text{CUE}}(\mathbf{c})$ over all other (complex) components,

$$P_N^{\text{CUE}}(y) = \int \delta(y - |c_0|^2) P_N^{\text{CUE}}(\mathbf{c}) \, d^2 c_0 \cdots d^2 c_{N-1} = (N-1)(1-y)^{N-2} \quad . \quad (33)$$

Again as for the COE, the mean of $P_N^{\text{CUE}}(y)$ is $1/N$ and the rescaling $\eta := yN$ leads to

$$P_N^{\text{CUE}}(\eta) = \frac{N-1}{N} \left(1 - \frac{\eta}{N} \right)^{N-2} \quad (34)$$

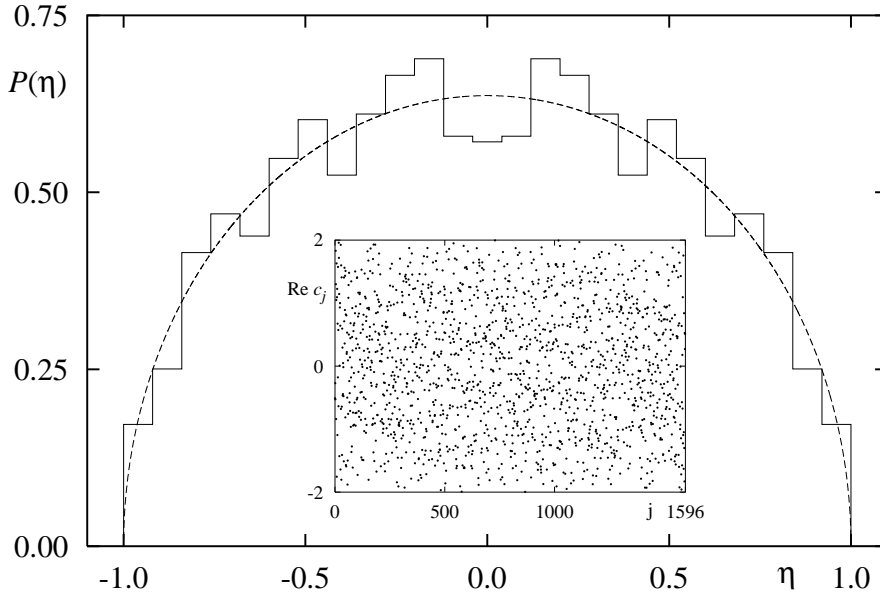


Figure 8: Eigenvector distribution of an eigenvector for the unperturbed (i.e. $\kappa = 0$) cat map (9) with $N = 1597$. This is compared with the asymptotic semicircle law, eq. (37). The inset shows the corresponding eigenvector (compare with the eigenvectors shown in the previous two figures).

which has mean 1. In the large N limit we have

$$P^{\text{CUE}}(\eta) = \exp(-\eta) . \quad (35)$$

and the cumulative distribution simply is

$$I^{\text{CUE}}(\eta) = 1 - \exp(-\eta) . \quad (36)$$

Fig. 7 shows $P(\eta)$ for one eigenvector of the perturbed cat map (22). There is good agreement with $P^{\text{CUE}}(\eta)$.

A different distribution is obtained for unperturbed cat maps: for certain subsequences of prime numbers (which depend on the map) the distribution of $\eta = \frac{1}{2}\text{Re } \psi$ tends to the semicircle law,

$$P(\psi) = \begin{cases} \frac{2}{\pi} \sqrt{1 - \eta^2} & \text{for } \eta \leq 1 \\ 0 & \text{for } \eta > 1 \end{cases} , \quad (37)$$

see [34] for details (see also [35]). In fig. 8 we show an example of an eigenstate with $N = 1597$ for the quantum map corresponding to the map (9) with $\kappa = 0$. For this N the map fulfils the conditions of [34] and one observes a nice semicircle distribution of the eigenvector. However, it seems that the approach to the asymptotic distribution is slower than for the case of the random matrix situations.

2.4.2 Husimi functions

A different representation of eigenstates is to consider a phase space representation, like for example the Husimi function, which allows for a more direct comparison with the structures for the classical map. Without going into the mathematical details, the Husimi representation is obtained by projecting the eigenstate onto a coherent state centred in a point $(q, p) \in \mathbb{T}^2$,

$$\begin{aligned} H_n(q, p) &= |\langle C_{q,p} | \psi_n \rangle|^2 = \left| \sum_{j=0}^{N-1} \langle C_{q,p} | q_j \rangle \langle q_j | \psi \rangle \right|^2 = \left| \sum_{j=0}^{N-1} \langle C_{q,p} | q_j \rangle c_j \right|^2 \\ &= \left| \sum_{j=0}^{N-1} (2N)^{1/4} \exp(-\pi N(q^2 - ipq)) \exp(\pi N(-q_j^2 + 2(q - ip)q_j)) \right. \\ &\quad \left. \vartheta_3 \left(i\pi N \left(q_j - \frac{i\theta_1}{N} - q + ip \right) \middle| iN \right) c_j \right|^2 . \end{aligned} \quad (38)$$

Here $q_j = \frac{1}{N}(\theta_2 + j)$, $j = 0, \dots, N-1$ and $\vartheta_3(Z|\tau)$ is the Jacobi-Theta function,

$$\vartheta_3(Z|\tau) = \sum_{n \in \mathbb{Z}} e^{i\pi\tau n^2 + 2inZ} , \quad \text{with } Z, \tau \in \mathbb{C}, \text{ Im}(\tau) > 0 . \quad (39)$$

The coefficients c_j are the components of the eigenvector ψ_n in the position representation as obtained from the diagonalization of U_N (for other generating functions than the one used in eq. (14) one has to adapt eq. (38)).

If one wants to compute a Husimi function on a grid of $N \times N$ points on \mathbb{T}^2 the computational effort grows with N^3 . So for computing all Husimi function of a quantum map for a given N the

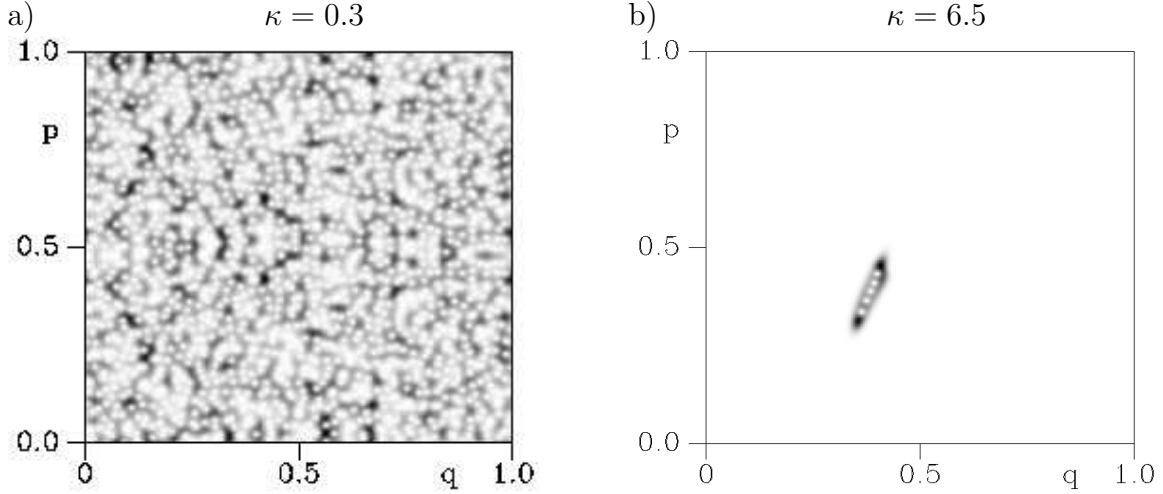


Figure 9: In a) a Husimi function $H_n(q, p)$ of the perturbed cat map (9) with $\kappa = 0.3$ is plotted which shows the expected ‘uniform’ distribution. Here black corresponds to large values of $H_n(q, p)$. In b) for $\kappa = 6.5$ a state localizing on one of the elliptic islands is shown (compare with fig. 2).

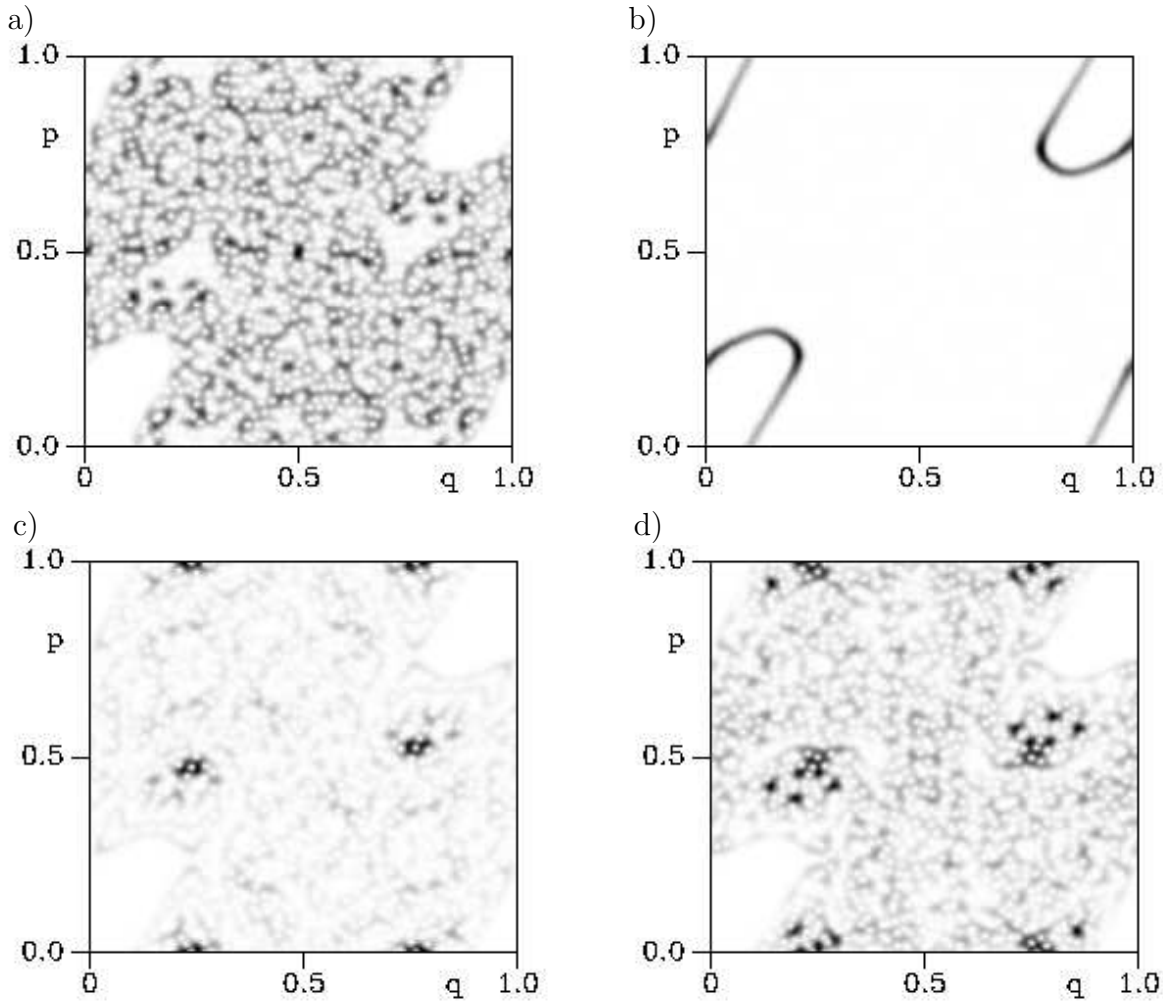


Figure 10: Examples of Husimi functions for the standard map with $\kappa = 3.0$ and $N = 1600$.

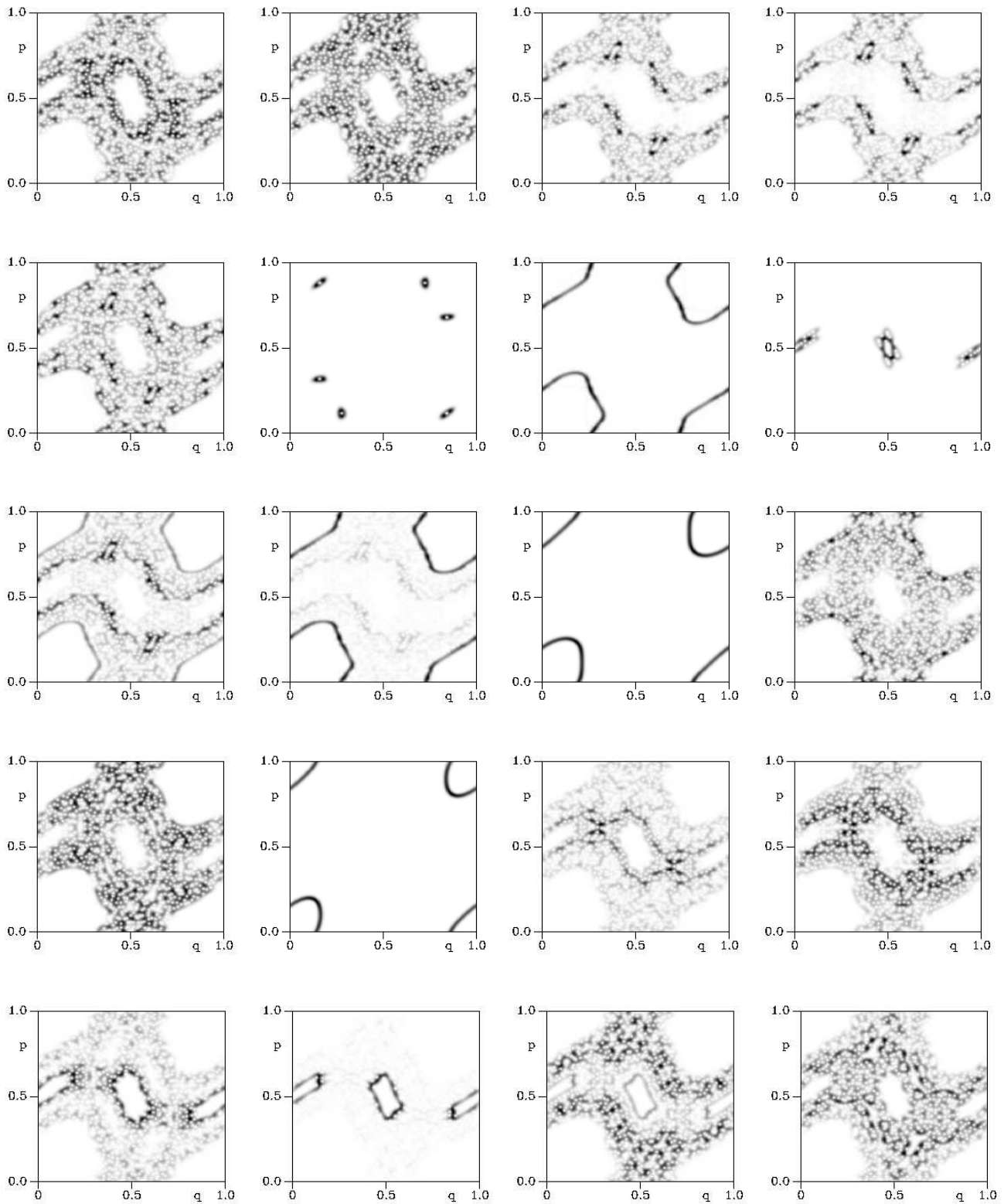


Figure 11: Examples of Husimi functions $H_n(q, p)$ for the standard map with $\kappa = 1.5$ and $N = 1600$ for $n = 0, \dots, 19$. (Compare with fig. 1.)

computational effort grows with N^4 . Already for moderate N this can be quite time-consuming, but even more importantly, usually one also wants to store all these Husimi functions on the hard-disk which limits the accessible range of N . Sometimes a smaller grid, e.g. of size $10\sqrt{N} \times 10\sqrt{N}$ can be sufficient which reduces the growth of the computational effort to N^2 for a single Husimi function and to N^3 for all Husimi functions at a given N . Even then one still needs $800 N^2$ Bytes to store these on the hard-disk. For example for $N = 1600$ this roughly leads to 2 GB of data and for $N = 3000$ one needs approximately 7 GB. However, there are also cases where a finer grid, e.g. $2N \times 2N$ is necessary.

Theoretically one expects that for $N \rightarrow \infty$ the Husimi functions concentrate on those regions in phase space which are invariant under the map (this follows from the Egorov property). So for ergodic systems the expectation is that (in the weak sense)

$$H_n(q, p) \rightarrow 1 \quad \text{with } n = 0, \dots, N-1 \text{ as the matrix size } N \rightarrow \infty . \quad (40)$$

The precise formulation of this statement is the contents of the quantum ergodicity theorem for maps [36] (see [37] for the case of discontinuous maps). The quantum ergodicity theorem only makes a statement about a subsequence of density one (i.e. almost all states) which for example leaves space for scars, i.e. eigenstates localized on unstable periodic orbits. For systems with mixed phase space one (asymptotically) expects localization in the stochastic region(s) and on the tori in the elliptic regions.

In fig. 9a) we show for the perturbed cat map with $\kappa = 0.3$ the Husimi function for the same eigenstate as in fig. 6. As expected it shows a quite uniform distribution (of course with the usual fluctuations). In contrast for $\kappa = 6.5$ there are eigenstates such as the one shown in fig. 9b) which localizes on the elliptic island (compare with fig. 2).

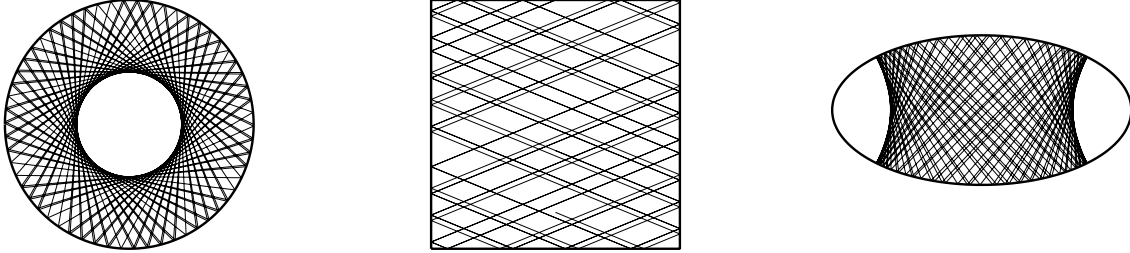
In some sense more interesting are the Husimi functions for mixed systems as the classical dynamics shows more structure. In fig. 10 we show some examples for the standard map with $\kappa = 3.0$ Fig. 10a) shows a Husimi function which is spread out in the irregular component. In contrast in b) the Husimi function localizes on a torus around the elliptic fixpoint. The Husimi function in c) shows quite strong localization around the small elliptic island of a periodic orbit with period 4. This island is so small that it is not visible in fig. 1. Therefore, the Husimi function displayed in fig. 10d) indicates that the region of ‘influence’ of this island is much larger than the area of the island. This region is also visible in the Husimi function in fig. 10a), as the irregular state has a very small probability in the regions around these islands. A longer sequence of Husimi functions for the standard map with $\kappa = 1.5$ shown in fig. 11 illustrates the different types of localized states (compare with fig. 1).

3 Billiards

3.1 Classical billiards

A two-dimensional Euclidean billiard is given by the free motion of a point particle in some domain $\Omega \subset \mathbb{R}^2$ with elastic reflections at the boundary $\partial\Omega$. Depending on the boundary one obtains completely different dynamical behaviour, see fig. 12 where this is illustrated by showing orbits of billiards in a circle, a square and an ellipse, which are all integrable giving rise to regular motion. In contrast the Sinai billiard (motion in a square with a circular scatterer), the stadium billiard (two semicircles joined by parallel straight lines) and the cardioid billiard show strongly chaotic motion (they are all proven to be hyperbolic, ergodic, mixing and K -systems).

Integrable systems



Chaotic systems

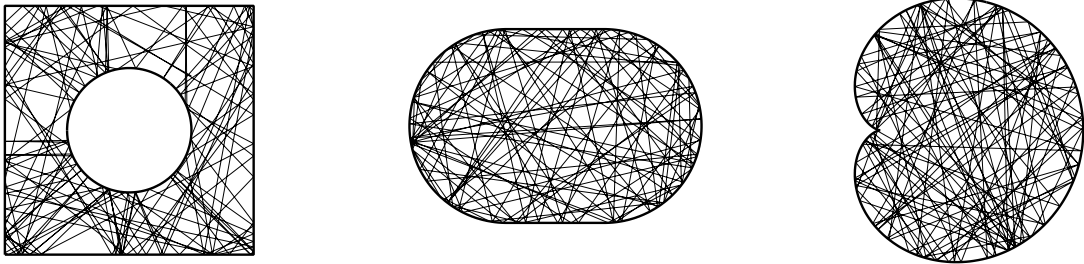


Figure 12: Billiard dynamics in integrable and chaotic systems.

As the motion inside the billiard is on straight lines it is convenient to use the boundary to define a Poincaré section,

$$\mathcal{P} := \{(s, p) \mid s \in [0, |\partial\Omega|], p \in [-1, 1]\} . \quad (41)$$

Here s is the arclength along $\partial\Omega$ and $p = \langle \mathbf{v}, \mathbf{T}(s) \rangle$ is the projection of the unit velocity vector \mathbf{v} after the reflection on the unit tangent vector $\mathbf{T}(s)$ in the point $s \in \partial\Omega$. The Poincaré map is then given by

$$\begin{aligned} P : \mathcal{P} &\rightarrow \mathcal{P} \\ \xi = (s, p) &\mapsto \xi' = (s', p') , \end{aligned}$$

i.e. for a given point $\xi = (s, p)$ one considers the ray starting at the point $\mathbf{r}(s) \in \partial\Omega$ in the direction specified by p and determines the first intersection with the boundary, leading to the new point $\xi' = (s', p')$. Explicitly, the Cartesian components of the unit velocity \mathbf{v} of a point particle starting on $\partial\Omega$ at $\mathbf{r}(s)$ are determined by the angle $\beta \in [-\pi/2, \pi/2]$ measured with respect to the inward pointing normal $\mathbf{N} = (-T_y, T_x)$. The velocity in the \mathbf{T}, \mathbf{N} coordinate system is denoted by $(p, n) = (\sin \beta, \cos \beta)$, so that in Cartesian coordinates

$$\mathbf{v} = (v_x, v_y) = \begin{pmatrix} T_x & N_x \\ T_y & N_y \end{pmatrix} (p, n) = \left(T_x p + N_x \sqrt{1 - p^2}, T_y p + N_y \sqrt{1 - p^2} \right) . \quad (42)$$

Starting in the point $\mathbf{r}(s) \in \partial\Omega$ in the direction \mathbf{v} , the ray $\mathbf{r} + t\mathbf{v}$ intersects $\partial\Omega$ at some point $\mathbf{r}' = (x', y')$. If the boundary is determined by the implicit equation

$$F(x, y) = 0 , \quad (43)$$

the new point \mathbf{r}' can be determined by solving

$$F(x + tv_x, y + tv_y) = 0 . \quad (44)$$

For non-convex billiards there are points $\xi = (s, p) \in \mathcal{P}$ for which there is more than one solution (apart from $t = 0$); obviously the one with the smallest $t > 0$ has to be chosen. The condition (43) can be used to remove the $t = 0$ solution analytically from (44). If F is a polynomial in x and y this allows to reduce the order of (44) by one. This approach has for example been used for the cardioid billiard leading to a cubic equation for t , see [38] for details. From the solution t one gets the coordinates $(x', y') = (x, y) + t\mathbf{v}$ which have to be converted (in a system dependent way) to the arclength coordinate s' (in many practical applications there is a more suitable internal variable, for example the polar angle etc.). The corresponding new projection of the momentum is given by $p' = -\langle \mathbf{v}, \mathbf{T}(s') \rangle$.

3.2 Quantum billiards

For a classical billiard system the associated quantum billiard is given by the stationary Schrödinger equation (in units $\hbar = 2m = 1$)

$$-\Delta\psi_n(\mathbf{q}) = E_n\psi_n(\mathbf{q}) , \quad \mathbf{q} \in \Omega \quad (45)$$

with (for example) Dirichlet boundary conditions, i.e. $\psi_n(\mathbf{q}) = 0$ for $\mathbf{q} \in \partial\Omega$. Here Δ denotes the Laplace operator, which reads in two dimensions

$$\Delta = \left(\frac{\partial^2}{\partial q_1^2} + \frac{\partial^2}{\partial q_2^2} \right) . \quad (46)$$

In the Schrödinger representation the state of a particle is described in configuration space by a wave function $\psi \in L^2(\Omega)$, where $L^2(\Omega)$ is the Hilbert space of square integrable functions on Ω . The interpretation of ψ is that $\int_D |\psi(\mathbf{q})|^2 d^2q$ is the probability of finding the particle inside the domain $D \subset \Omega$.

Due to the compactness of Ω , the quantal energy spectrum $\{E_n\}$ is purely discrete and can be ordered as $0 < E_1 \leq E_2 \leq E_3 \leq \dots$. The eigenfunctions can be chosen to be real and to form an orthonormal basis of $L^2(\Omega)$,

$$\langle \psi_n | \psi_m \rangle := \int_{\Omega} \psi_n(\mathbf{q}) \psi_m(\mathbf{q}) d^2q = \delta_{mn} .$$

The mathematical problem defined by eq. (45) is the well-known eigenvalue problem of the Helmholtz equation, which for example also describes a vibrating membrane or flat microwave cavities. For some simple domains Ω it is possible to solve eq. (45) analytically. For example for the billiard in a rectangle with sides a and b the (non-normalized) eigenfunctions are given by $\psi_{n_1, n_2}(\mathbf{q}) = \sin(\pi n_1 q_1/a) \sin(\pi n_2 q_2/b)$ with corresponding eigenvalues $E_{n_1, n_2} = \pi^2(n_1^2/a^2 + n_2^2/b^2)$ and $(n_1, n_2) \in \mathbb{N}^2$. For the billiard in a circle the eigenfunctions are given in polar-coordinates

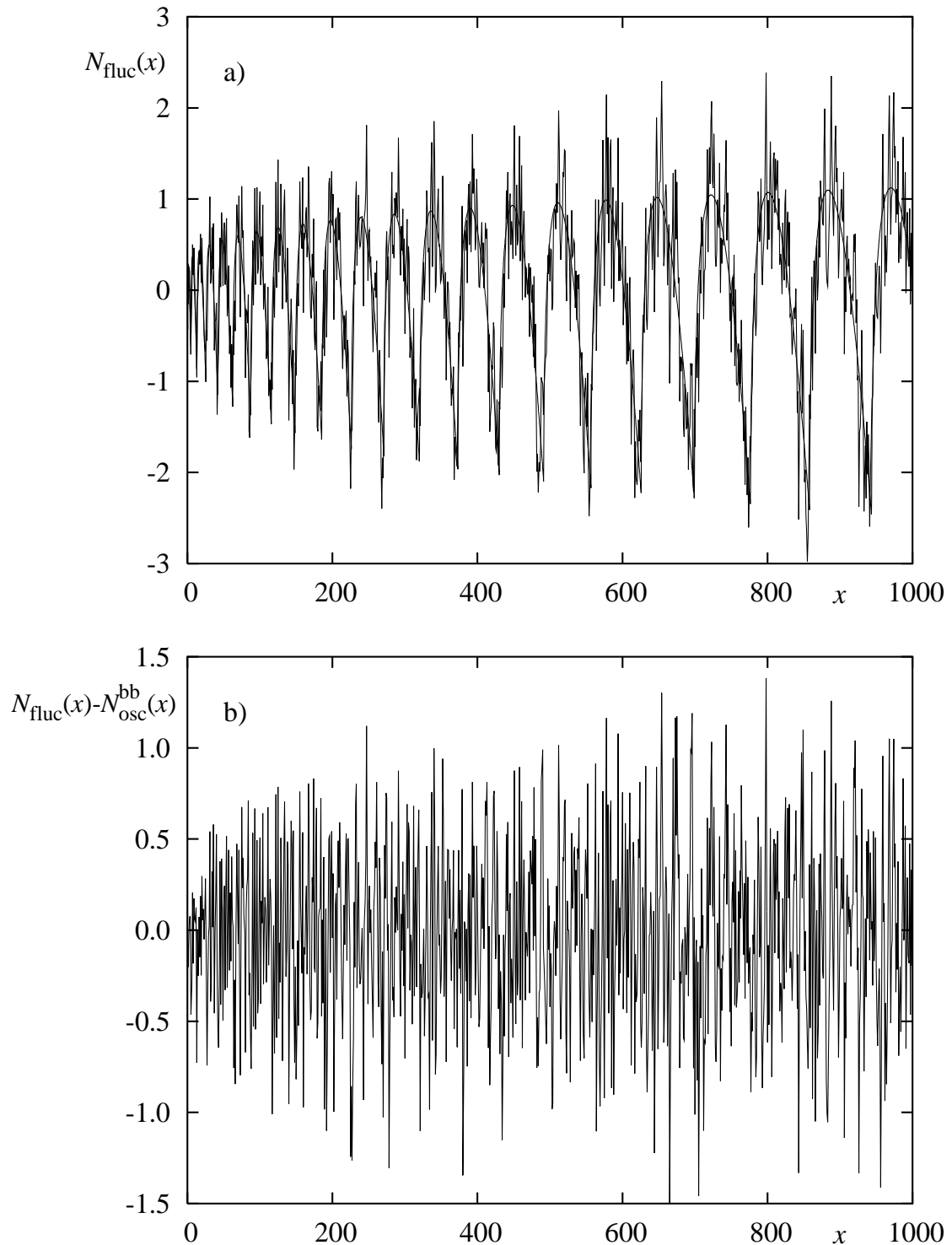


Figure 13: Plot of $N_{\text{fluc}}(x)$ for the stadium billiard ($a = 1.8$, odd-odd symmetry) together with the contribution from the bouncing ball orbits, dashed line, see eq. (52). In b) the fluctuating part after subtraction of the contribution of the bouncing ball orbits is shown.

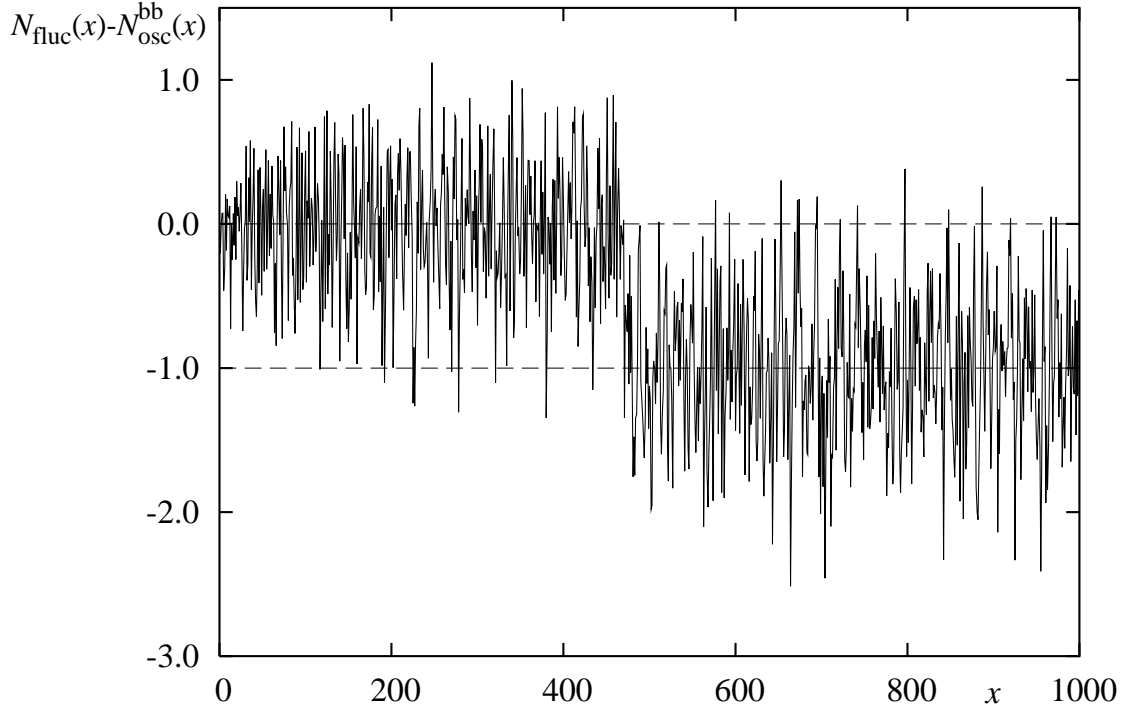


Figure 14: Detection of missing levels using the δ_n -statistics. Shown is $N_{\text{fluc}}(x) - N_{\text{osc}}^{\text{bb}}(x)$ for the case where one level has been removed from the spectrum. One clearly sees the jump in the fluctuations which allows to roughly locate the place where the level is missing.

by $\psi_{mn}(r, \varphi) = J_m(j_{mn}r) \exp(im\varphi)$, where j_{mn} is the n -th zero of the Bessel function $J_m(x)$ and $m \in \mathbb{Z}$, $n \in \mathbb{N}$. However, in general no analytical solutions of eq. (45) exist so that numerical methods have to be used to compute eigenvalues and eigenfunctions.

The spectral staircase function $N(E)$ (integrated level density)

$$N(E) := \#\{n \mid E_n \leq E\} \quad (47)$$

counts the number of energy levels E_n below a given energy E . $N(E)$ can be separated into a mean smooth part $\overline{N}(E)$ and a fluctuating part

$$N(E) = \overline{N}(E) + N_{\text{fluc}}(E) . \quad (48)$$

For two-dimensional billiards, $\overline{N}(E)$ is given by the generalized Weyl formula [39]

$$\overline{N}(E) = \frac{\mathcal{A}}{4\pi}E - \frac{\mathcal{L}}{4\pi}\sqrt{E} + \mathcal{C} + \dots , \quad (49)$$

where \mathcal{A} denotes the area of the billiard, and $\mathcal{L} := \mathcal{L}^- - \mathcal{L}^+$, where \mathcal{L}^- and \mathcal{L}^+ are the lengths of the pieces of the boundary $\partial\Omega$ with Dirichlet and Neumann boundary conditions, respectively. The constant \mathcal{C} takes curvature and corner corrections into account.

The simplest quantity is the δ_n -statistics, which is obtained from the fluctuating part of the spectral staircase evaluated at the unfolded energy eigenvalues $x_n := \overline{N}(E_n)$

$$\delta_n := N_0(E_n) - \overline{N}(E_n) = n - \frac{1}{2} - x_n , \quad (50)$$

where

$$N_0(E) := \lim_{\epsilon \rightarrow 0} \frac{N(E + \epsilon) + N(E - \epsilon)}{2} . \quad (51)$$

The quantity δ_n is a good measure for the completeness of a given energy spectrum. For a complete spectrum δ_n , or equivalently $N_{\text{fluc}}(x)$, should fluctuate around zero. Fig. 13a) shows $N_{\text{fluc}}(x)$ for the stadium billiard, which indeed fluctuates around zero. In addition there is an overall modulation of $N_{\text{fluc}}(x)$ which is caused by the bouncing ball orbits. They form a one parameter family of periodic orbits having perpendicular reflections at the two parallel walls (of length a , see fig. 15) of the stadium. The contribution of these orbits to the spectral staircase function reads [40]

$$N_{\text{fluc}}^{\text{bb}}(E) = \frac{a}{\pi} \sum_{n=1}^{\infty} \sqrt{E - E_n^{\text{bb}}} \Theta\left(\sqrt{E} - \sqrt{E_n^{\text{bb}}}\right) - \left(\frac{a}{4\pi}E - \frac{1}{2\pi}\sqrt{E}\right) \quad (52)$$

$$= \frac{a}{2\sqrt{\pi^3}} E^{\frac{1}{4}} \sum_{n=1}^{\infty} \frac{1}{n^{\frac{3}{2}}} \cos\left(2an\sqrt{E} - \frac{3\pi}{4}\right) , \quad (53)$$

where $E_n^{\text{bb}} = \pi^2 n^2$ are the eigenvalues of a particle in a one-dimensional box of length 1, and Θ is the Heaviside step function. Subtracting $N_{\text{osc}}^{\text{bb}}(x)$ from $N_{\text{fluc}}(x)$ removes the additional oscillation, see fig. 13b). If an eigenvalue is missing this is clearly visible by a ‘jump’ of δ_n in comparison to points fluctuating around 0, see fig. 14 for an example where one eigenvalue has been removed ‘by-hand’. Clearly, the energy interval in which a level is missing can be estimated from the plot.

In the same way as for quantum maps one can study the level spacing distribution and more complicated statistics, like the number variance, n -point correlation functions etc., see for example [41, 42] for some further examples for the cardioid billiard.

3.3 Computing eigenvalues and eigenfunctions for quantum billiards

There exist several numerical methods to solve the Helmholtz equation inside a domain $\Omega \subset \mathbb{R}^2$,

$$\Delta\psi(\mathbf{q}) + k^2\psi(\mathbf{q}) = 0 , \quad \mathbf{q} \in \Omega \setminus \partial\Omega , \quad (54)$$

with Dirichlet boundary conditions

$$\psi(\mathbf{q}) = 0 , \quad \mathbf{q} \in \partial\Omega . \quad (55)$$

For a good review on the determination of the eigenvalues of (54) see [43], which however does not cover finite element methods or boundary integral methods. Additionally, in the context of quantum chaos the plane wave decomposition [44] (see also [45] for a detailed description of the method), the scattering approach, see e.g. [46–48], and more recently the scaling method [49], are commonly used.

Here I will give a sketch of the derivation of the boundary integral method and discuss in more detail the numerical implementation. The boundary integral method reduces the problem of solving the two-dimensional Helmholtz equation (54) to a one-dimensional integral equation, see e.g. [50–65] and references therein. Of course, the general approach also applies to higher dimensions but we will only discuss the two-dimensional case. For studies of three-dimensional systems by various methods see e.g. [66–70]. Boundary integral methods are also used in many other areas so that it is impossible to give a full account. For example they are also commonly used in acoustics, see e.g. [71] and the detailed list of references therein. Finally, the boundary integral method provides a starting point to derive the Gutzwiller trace formula, see e.g. [72–75, 64].

3.3.1 Boundary integral equation

Let $G(\mathbf{q}, \mathbf{q}')$ be a Green function of the inhomogeneous equation, i.e.

$$(\Delta + k^2)G_k(\mathbf{q}, \mathbf{q}') = \delta(\mathbf{q} - \mathbf{q}') . \quad (56)$$

Considering the integral over Ω of the difference $\psi(\mathbf{q}') \cdot (56) - G_k(\mathbf{q}, \mathbf{q}') \cdot (54)$ one obtains

$$\int_{\Omega} [\psi(\mathbf{q}') \Delta' G_k(\mathbf{q}, \mathbf{q}') - G_k(\mathbf{q}, \mathbf{q}') \Delta' \psi(\mathbf{q}')] d^2 \mathbf{q}' = \int_{\Omega} \psi(\mathbf{q}') \delta(\mathbf{q} - \mathbf{q}') d^2 \mathbf{q}' . \quad (57)$$

Using the second Green theorem gives the Helmholtz representation

$$\oint_{\partial\Omega} \left[\psi(\mathbf{q}') \frac{\partial G_k}{\partial n'}(\mathbf{q}, \mathbf{q}') - G_k(\mathbf{q}, \mathbf{q}') \frac{\partial \psi}{\partial n'}(\mathbf{q}') \right] ds' = \begin{cases} \psi(\mathbf{q}) & ; \quad \mathbf{q} \in \Omega \setminus \partial\Omega \\ \frac{1}{2}\psi(\mathbf{q}) & ; \quad \mathbf{q} \in \partial\Omega \\ 0 & ; \quad \text{else} \end{cases} . \quad (58)$$

Here $\mathbf{q}' \equiv \mathbf{q}(s')$ and $\frac{\partial}{\partial n'} = \mathbf{n}(s') \nabla$ with $\mathbf{n}(s) = (q'_2(s), -q'_1(s))$ denoting the outward pointing normal vector, where $(q_1(s), q_2(s))$ is a parametrization of the billiard boundary $\partial\Omega$ in terms of the arclength s , oriented counterclockwise. Special care has to be taken to obtain the result for $\mathbf{q} \in \partial\Omega$, see e.g. [51, 74]. (When \mathbf{q} is in a corner of the billiard the factor $\frac{1}{2}$ has to be replaced by $\frac{\theta}{2\pi}$, where θ is the (inner) angle of the corner.) For Dirichlet boundary conditions one obtains

$$\oint_{\partial\Omega} u(s') G_k(\mathbf{q}, \mathbf{q}') ds' = 0 , \quad \mathbf{q} \in \partial\Omega , \quad (59)$$

where

$$u(s) := \frac{\partial}{\partial n} \psi(\mathbf{q}(s)) := \mathbf{n}(s) \nabla \psi(\mathbf{q}(s)) := \mathbf{n}(s) \lim_{\substack{\mathbf{q}' \rightarrow \mathbf{q}(s) \\ \mathbf{q}' \in \Omega \setminus \partial\Omega}} \nabla \psi(\mathbf{q}') \quad (60)$$

is the normal derivative function of ψ .

In two dimensions a Green function for a free particle is given by the Hankel function of first kind

$$G_k(\mathbf{q}, \mathbf{q}') = -\frac{i}{4} H_0^{(1)}(k|\mathbf{q} - \mathbf{q}'|) = -\frac{i}{4} [J_0(k|\mathbf{q} - \mathbf{q}'|) + i Y_0(k|\mathbf{q} - \mathbf{q}'|)] . \quad (61)$$

Since $H_0^{(1)}(z) \sim \frac{i}{\pi} \ln z$ for $z \rightarrow 0$, the Green function $G_k(\mathbf{q}, \mathbf{q}')$ diverges logarithmically such that it is more convenient to derive an integral equation whose kernel is free of this singularity. To that end one (formally) applies the normal derivative $\frac{\partial}{\partial n}$ to eq. (58). More carefully one has to consider a jump relation for the normal derivative function, see e.g. [51, 74]. The result is

$$u(s) = -2 \oint_{\partial\Omega} \frac{\partial}{\partial n} G_k(\mathbf{q}(s), \mathbf{q}(s')) u(s') ds' . \quad (62)$$

For the derivative of the Green function one obtains

$$\frac{\partial}{\partial n} G_k(\mathbf{q}(s), \mathbf{q}(s')) = \frac{ik}{4} \cos(\phi(s, s')) H_1^{(1)}(k\tau(s, s')) , \quad (63)$$

where $\tau(s, s') = |\mathbf{q}(s) - \mathbf{q}(s')|$ is the Euclidean distance between the two points on the boundary and

$$\cos \phi(s, s') = \frac{\mathbf{n}(s) (\mathbf{q}(s) - \mathbf{q}(s'))}{\tau(s, s')} . \quad (64)$$

This gives the integral equation for the normal derivative $u(s)$

$$u(s) = \oint_{\partial\Omega} Q_k(s, s') u(s') \, ds' , \quad (65)$$

with integral kernel

$$Q_k(s, s') = -\frac{ik}{2} \cos \phi(s, s') H_1^{(1)}(k \tau(s, s')) . \quad (66)$$

Eq. (65) is a Fredholm equation of second kind which has non-trivial solutions if the determinant

$$D(k) := \det(\mathbb{1} - \hat{Q}_k) \quad (67)$$

vanishes. Here \hat{Q}_k is the integral operator on $\partial\Omega$ defined by

$$\hat{Q}_k(u(s)) = \oint_{\partial\Omega} Q_k(s, s') u(s') \, ds' . \quad (68)$$

For eigenvalues E_n of the Helmholtz equation with Dirichlet boundary conditions one has $D(k) = 0$ for $k = \sqrt{E_n}$, see e.g. [74] for a detailed proof. However, for $\text{Im } k < 0$ there can be further zeros of $D(k)$ which (for the interior Dirichlet problem) correspond to the outside scattering problem with Neumann boundary conditions [76–78] (see also [51]). Explicitly this can be seen from the factorization $D(k) = D(0)D_{\text{int}}(k)D_{\text{ext}}(k)$, where the factors can be written exclusively in terms of the interior and exterior problem. More aspects concerning the additional spurious solutions will be discussed in sec. 3.3.5.

Before turning to the numerical implementation, let us discuss the behaviour of the integral kernel for small arguments. The Hankel function $H_1^{(1)}(x)$ reads for small arguments

$$H_1^{(1)}(k \tau(s, s')) \sim -\frac{2i}{\pi k |s - s'|} , \quad \text{for } s - s' \rightarrow 0 . \quad (69)$$

This singularity is compensated by the behaviour of

$$\cos \phi(s, s') \sim -\frac{1}{2} \kappa(s) |s - s'| , \quad \text{for } s' \rightarrow s , \quad (70)$$

where $\kappa(s)$ is the curvature of the boundary in the point s . Here the curvature is defined by $\kappa(s) = q'_1(s)q''_2(s) - q'_2(s)q''_1(s)$ such that for example $\kappa(s) = 1$ for a circle of radius one. Thus for the integral kernel we obtain

$$Q_k(s, s') \rightarrow \frac{1}{2\pi} \kappa(s) , \quad \text{for } s - s' \rightarrow 0 . \quad (71)$$

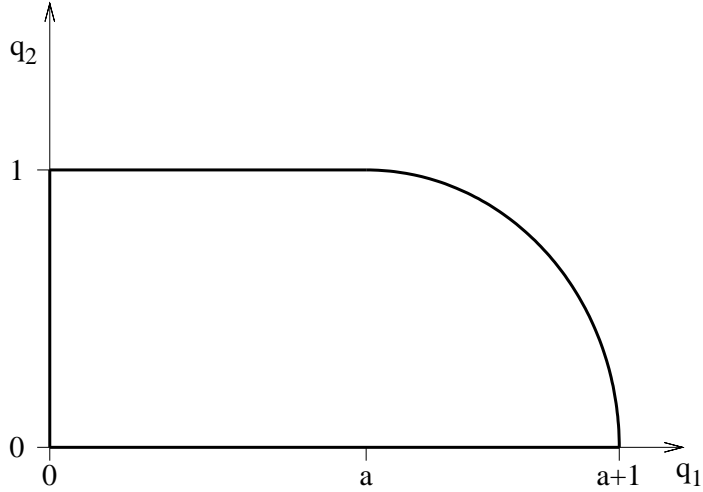


Figure 15: Geometry of the desymmetrized stadium billiard.

3.3.2 Desymmetrization

For systems with symmetries the numerical effort can be reduced by considering instead of the full system the symmetry reduced system with the corresponding Green function, see e.g. [56]. For a reflection symmetry with respect to the q_1 -axis one has

$$G_k^\pm(\mathbf{q}, \mathbf{q}') := G_k(|\mathbf{q} - \mathbf{q}'|) \pm G_k(|\mathbf{q} - (q'_1, -q'_2)|) , \quad (72)$$

where $+$ applies to the case of even eigenfunctions (i.e. Neumann boundary conditions on the symmetry axis) and $-$ to odd eigenfunctions (i.e. Dirichlet boundary conditions on the symmetry axis).

For a two-fold reflection symmetry (as in the case of the stadium billiard, see fig. 15 for a sketch of the geometry and notations) one has altogether four different subspectra, corresponding to DD, DN, ND and DD boundary conditions on the symmetry axes q_1 and q_2 , respectively. For example for Dirichlet-Dirichlet boundary conditions on the q_1 - and q_2 -axes the Green function reads

$$G_k^{\text{DD}} = G_k(|\mathbf{q} - \mathbf{q}'|) - G_k(|\mathbf{q} - (q'_1, -q'_2)|) + G_k(|\mathbf{q} - (-q'_1, -q'_2)|) - G_k(|\mathbf{q} - (-q'_1, q'_2)|) . \quad (73)$$

For Neuman boundary conditions on these two axes one gets

$$G_k^{\text{NN}} = G_k(|\mathbf{q} - \mathbf{q}'|) + G_k(|\mathbf{q} - (q'_1, -q'_2)|) + G_k(|\mathbf{q} - (-q'_1, -q'_2)|) + G_k(|\mathbf{q} - (-q'_1, q'_2)|) . \quad (74)$$

The advantage of exploiting the symmetries of the system is two-fold: firstly, we can separate the eigenvalues and eigenfunctions for the different symmetry classes, which is necessary for the investigation of the spectral statistics. Secondly, the numerical effort is reduced, since the integral over the whole boundary $\partial\Omega$ is reduced to an integral over a part of the boundary, which in the above examples is half or a quarter of the original boundary. The boundary along the symmetry axes need not be discretized as the boundary condition is already fulfilled by construction. Of course, for other geometries different choices for G can be more appropriate.

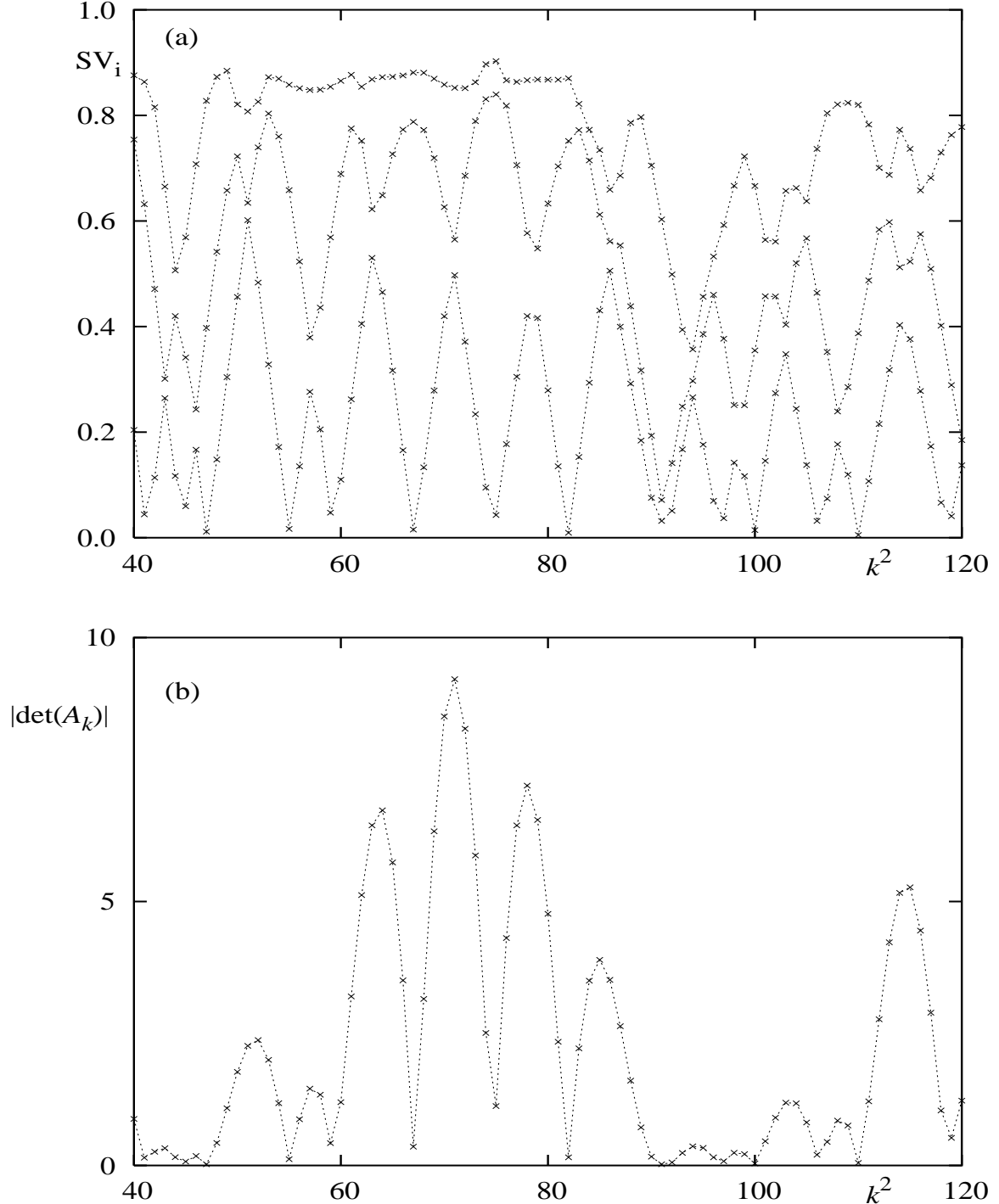


Figure 16: In a) the three smallest singular values are shown as a function of the energy $E = k^2$ for the stadium billiard with $a = 1.8$ and odd-odd symmetry. The eigenvalues are located at the minima of the first singular value. The second and third singular values allow to locate places with near degeneracies as next to $k^2 = 90$, which can be resolved by magnification of the corresponding region, see fig. 17. In b) $|\det(A_k)|$ is shown. The minima tend to be not as pronounced as those of the singular values.

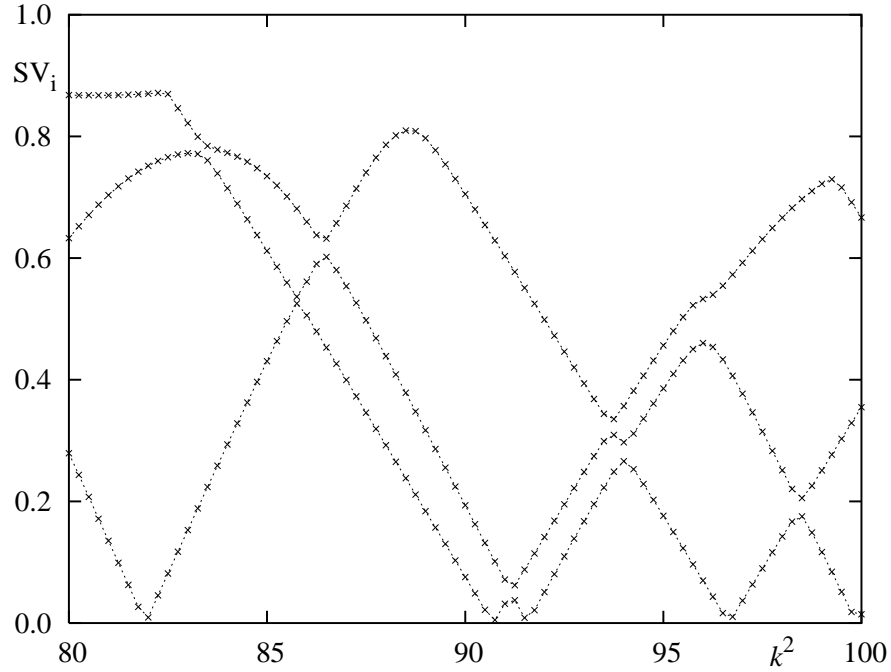


Figure 17: A magnification of fig. 16 shows that the singular value decomposition method easily allows to locate nearly degenerate energy levels.

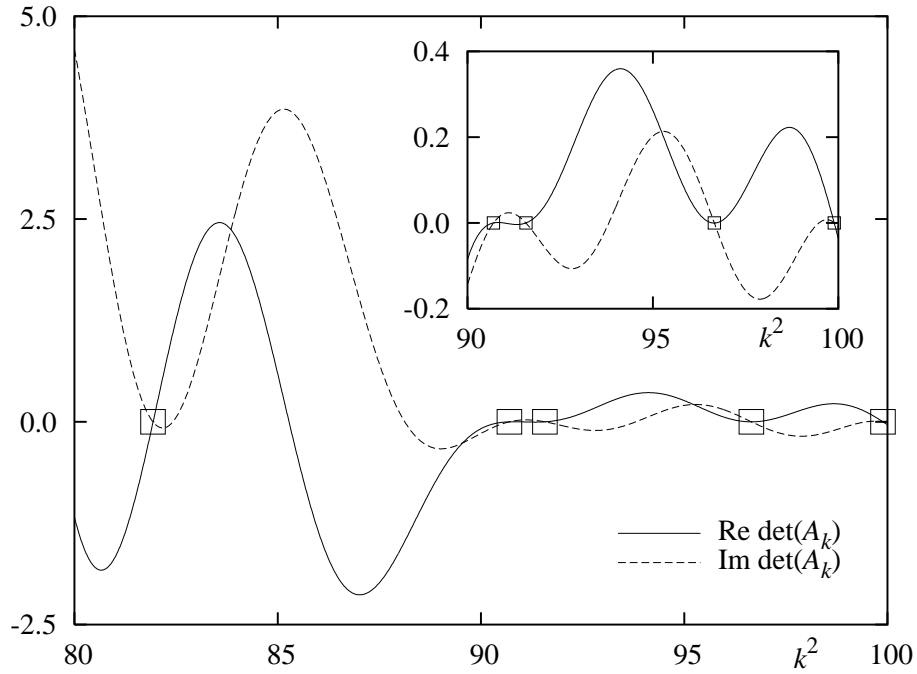


Figure 18: Plot of real and imaginary part of $\det(A_k)$ as a function of k ; the evaluation was done for 10 times as many points in k^2 than for fig. 17. Approximately simultaneous zeros correspond to minima of $|\det(A_k)|$. The locations of the eigenvalues are marked by squares.

3.3.3 Finding the eigenvalues

In the numerical computations the integral over the boundary is replaced by a Riemann sum. (There also exist more refined methods using polynomial approximations combined with Gauß-Legendre integration, see e.g. [60], which allow for a less fine discretization.) Let $\Delta s = \mathcal{L}/N$ be the discretization length of the boundary of length \mathcal{L} into N pieces. Then we have

$$u(s_i) = \Delta s \sum_{j=0}^{N-1} Q_k(s_i, s_j) u(s_j) , \quad (75)$$

where $s_i = (i + 1/2)\Delta s$, $i = 0, \dots, N - 1$. Equation (75) can be written in matrix form as

$$A_k \mathbf{u} = 0 , \quad \text{with} \quad A_{ij} = \delta_{ij} - \Delta s Q_k(s_i, s_j) . \quad (76)$$

Recall that for $s_i = s_j$ the kernel $Q_k(s_i, s_j)$ reduces to the result given in eq. (71). The solutions of this linear equation provide approximations to the eigenvalues k_n^2 and eigenvectors u_n . This leads to the problem of finding the real zeroes of the determinant

$$\det(A_k) = 0 \quad (77)$$

as a function of $k = \sqrt{E}$, where A_k is a dense, complex non-Hermitean matrix. Due to the discretization of the integral the determinant $\det(A_k)$ will not become zero but only close to zero (actually, the discretization shifts the zeros slightly away from the real axis, see [58, 59]).

In the numerical computations it is very useful [60] to compute the singular values of the matrix A instead of its determinant. The singular value decomposition of a complex matrix is given by the product of an unitary matrix U , a diagonal matrix S and a second unitary matrix V

$$A = USV^\dagger . \quad (78)$$

The diagonal matrix S contains as entries SV_i the singular values of A and we have $|\det A| = |\prod SV_i|$. Since the original integral equation has been discretized, the smallest singular value in general never gets zero, but just very small, see fig. 16. Thus the minima of the smallest singular value provide approximations to the eigenvalues of the integral equation. For the numerical computation of the singular value decomposition one may for example use the NAG routine F02XEF or the LAPACK routines ZGESVD or ZGESDD. It turns out that the (more recent) routine ZGESDD is significantly faster (factor 3-5, at the expense of a higher memory consumption), in particular when also singular vectors are computed.

The advantage of the singular value decomposition in comparison to locating the zeros of the determinant is that degeneracies of eigenvalues can be detected by looking at the second singular value, which also gets small when there are two nearby eigenvalues (similarly higher degeneracies can be found by looking at the next singular values). In fig. 16a) an example of the behaviour of the three smallest singular values is shown in the case of the stadium billiard ($a = 1.8$) with Dirichlet boundary conditions. For comparison a plot of $|\det(A_k)|$ is shown in fig. 16b). One clearly sees that the singular value decomposition provides more information. For example, next to $k^2 = 90$ the minimum of $|\det(A_k)|$ looks slightly broader than the others, however, this does not give a clear indication that there might be more than one eigenvalue. In contrast, the singular value decomposition method allows to resolve such kind of near-degeneracies efficiently, see fig. 17. Of course, this information is also available via $\det(A_k)$, see fig. 18 where its real and imaginary

part are plotted separately. Here (approximately) simultaneous zeros correspond to minima of $|\det(A_k)|$. However, notice that compared to the singular value decomposition approach much more discretization points in $E = k^2$ are necessary.

To determine all energy levels in a given energy interval $[E_1, E_2]$ one proceeds in the following way: first one computes the singular values at equidistantly chosen points $k^2 \in [E_1, E_2]$; the energy is chosen as variable because for two-dimensional billiards the mean distance between two energy levels is approximately constant and according to the generalized Weyl formula (49) given by $\frac{4\pi}{A}$. The finer the step size is chosen the easier the minima can be resolved, however, at the same time the computing time to cover a given energy range increases correspondingly. The actual step size is a compromise between these two aspects; good results have been achieved by using a step size of the order of $\frac{1}{5} \frac{4\pi}{A}$ (for systems with many near level degeneracies, e.g. integrable or near-integrable systems, a smaller step size can be helpful).

The matrix size N is chosen according to $N = b \frac{\mathcal{L}}{\lambda} = b \frac{\mathcal{L} k}{2\pi}$, such that one obtains b discretization points per units of the inverse of the de Broglie wave length $\lambda = \frac{2\pi}{k}$ along the boundary \mathcal{L} . Typical choices for b are between 5 and 12 depending on the system and the wanted accuracy.

From the first scan one locates all minima of the smallest singular value. If also the second singular value has a minimum next to a minimum of the first one, one has to use a refined discretization in E around the minimum (the numerical implementation is a bit more sophisticated, in order to account for several special situations, so that only a minimal number of additional points need to be computed). Once an isolated minimum is found, an approximation to the eigenvalue can be computed by different methods. Either one can perform a refined computation around the minimum, which can be quite time-consuming, or one can use a local approximation by a parabola [79]. A linear interpolation also gives good results: From the three points 1: $(k_1^2, SV_1(k_1^2))$, 2: $(k_2^2, SV_1(k_2^2))$, 3: $(k_3^2, SV_1(k_3^2))$, characterizing a minimum of the first singular value, one has two

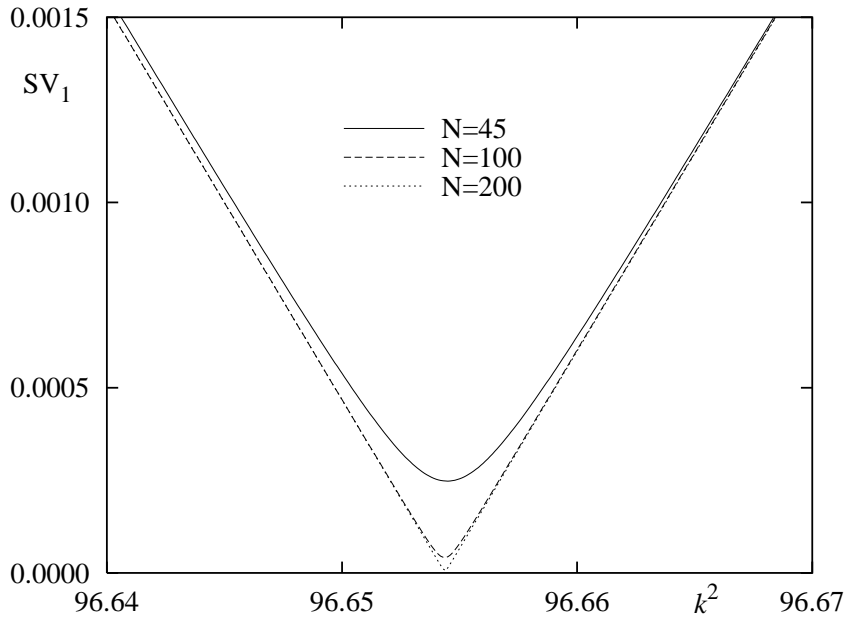


Figure 19: Magnification of fig. 17 around the minimum with $k^2 \approx 96.5$ for different matrix sizes N . One nicely sees the pronounced parabolic structure for $N = 45$ which gets smaller for larger N .

different lines $\overline{12}$ and $\overline{23}$ with different slopes, of which the line with the larger slope has to be chosen. The intersection of this line with the zero axis gives a good approximation to the eigenvalue, which one can refine if necessary. By repeatedly applying this for all minima, all energy levels in a given interval can be found. In fact, it is possible to develop a computer program which takes care of all this such that all levels can be found automatically.

A good check of the completeness is provided by considering the δ_n statistics, see the example in sec. 3.2. The accuracy of the computed eigenvalues can be estimated from the bracket of the minimum given by the three points 1,2,3 if the matrix dimension N is large enough. For N too small (for a given resolution in E) one does not obtain a peaked, but a broad minimum. This is illustrated in fig. 19 by magnifying fig. 17 around the minimum with $k^2 \approx 96.5$ for different N . One clearly sees the parabolic structure around the minimum for smaller N and for larger N one recovers the essentially linear behaviour of the smallest singular value.

Tests of the accuracy of the method can be obtained by considering a system where the eigenvalues are known. For example for the circular billiard the eigenvalues can be computed with arbitrary accuracy. Also billiards where the eigenvalues can be computed by other methods (e.g. conformal mapping method [80, 81]) allow a determination of the accuracy of the method. For a study of the scaling of the error for various billiards see [63]. In addition computations of the normal derivative function $u_n(s)$ and the eigenfunction (both inside and outside of Ω) allow to check the quality of the numerical method and program.

3.3.4 Computing eigenfunctions

From a minimum of the smallest singular value we obtain an approximation of the eigenvalue and at the same time the corresponding singular vector \mathbf{u} gives an approximation to the normal derivative function $u(s)$. The NAG routine F02XEF scales the singular vector such that its first component is real. Thus for a correct solution also the other components should be essentially real, which provides another check for the implementation of the method and the accuracy of the eigenvalues.

The eigenfunction in the interior of the domain Ω can now be calculated from the normal derivative function,

$$\psi(\mathbf{q}) = -\frac{i}{4} \oint_{\partial\Omega} H_0^{(1)}(k|\mathbf{q} - \mathbf{q}(s)|) u(s) \, ds , \quad \text{for } \mathbf{q} \in \Omega \setminus \partial\Omega . \quad (79)$$

The computation of the eigenfunction can be simplified by taking into account that

$$\oint_{\partial\Omega} J_0(k|\mathbf{q} - \mathbf{q}(s)|) u(s) \, ds = 0 , \quad (80)$$

because the J_0 -part of $G_k(\mathbf{q}, \mathbf{q}')$ is a solution of the homogeneous equation corresponding to eq. (56). Thus (79) is equivalent to

$$\psi(\mathbf{q}) = \frac{1}{4} \oint_{\partial\Omega} Y_0(k|\mathbf{q} - \mathbf{q}(s)|) u(s) \, ds , \quad \text{for } \mathbf{q} \in \Omega \setminus \partial\Omega . \quad (81)$$

If one uses a desymmetrization, such as eq. (72), (73) or (74), the above formula (81) has to be modified accordingly.

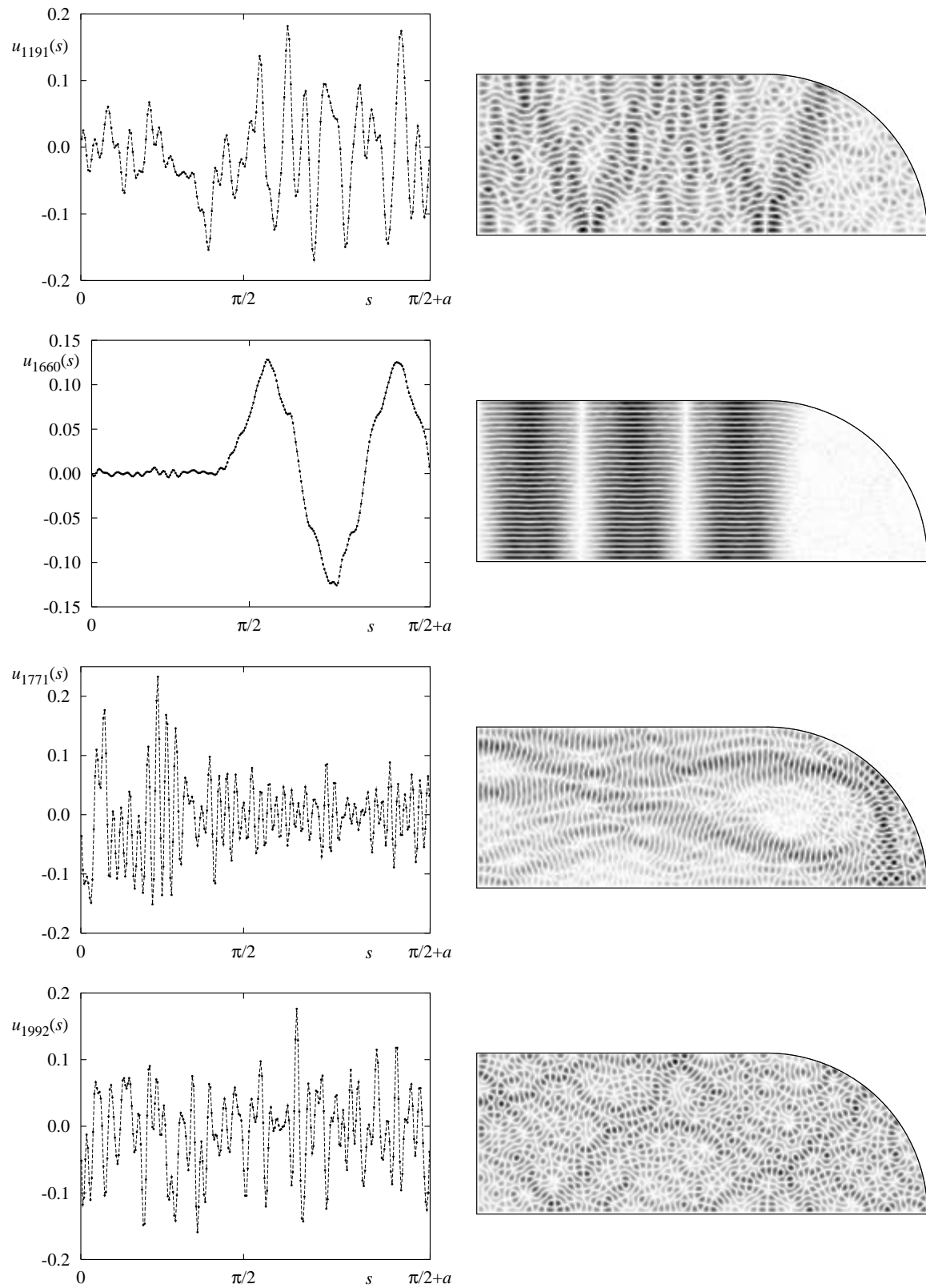


Figure 20: Examples of normal derivative functions $u_n(s)$ and the corresponding eigenfunctions in the stadium billiard (odd-odd symmetry, $a = 1.8$). Here black corresponds to high intensity of $|\psi_n(\mathbf{q})|^2$.

In fig. 20 we show some examples of normal derivatives $u_n(s)$ and the corresponding eigenfunctions of the billiard, computed via eq. (81). The imaginary part of $u_n(s)$ is typically 5 or more orders of magnitude smaller than the real part. It is interesting to see that part of the structure of the eigenfunctions is also reflected in $u_n(s)$. For example for eigenstates with small probability in the region of the quarter circle also the normal derivative is small for $s < \pi/2$.

3.3.5 Spurious solutions I: Real Green function approach

In certain situations and for some numerical methods it may happen that one obtains in addition to the true solutions of the Helmholtz equation (54) further so-called *spurious solutions*. This question is discussed in some of the papers on the boundary integral method, in particular see [50, 52, 53] and [55, 58]. There are essentially two different situations in which they are encountered. The first is that one uses for the Green function instead of the Hankel function, see eq. (61), just the real part, i.e.

$$G_k(\mathbf{q}, \mathbf{q}') = \frac{1}{4} Y_0(k |\mathbf{q} - \mathbf{q}'|) . \quad (82)$$

This seems reasonable as according to (80) the J_0 -Bessel function does not contribute to the eigenfunction. Moreover then one can work with an entirely real matrix for which the singular value decomposition can be computed much faster. However, when using this approach, there appear additional zeros (for each correct one there is one additional one) and the singular values

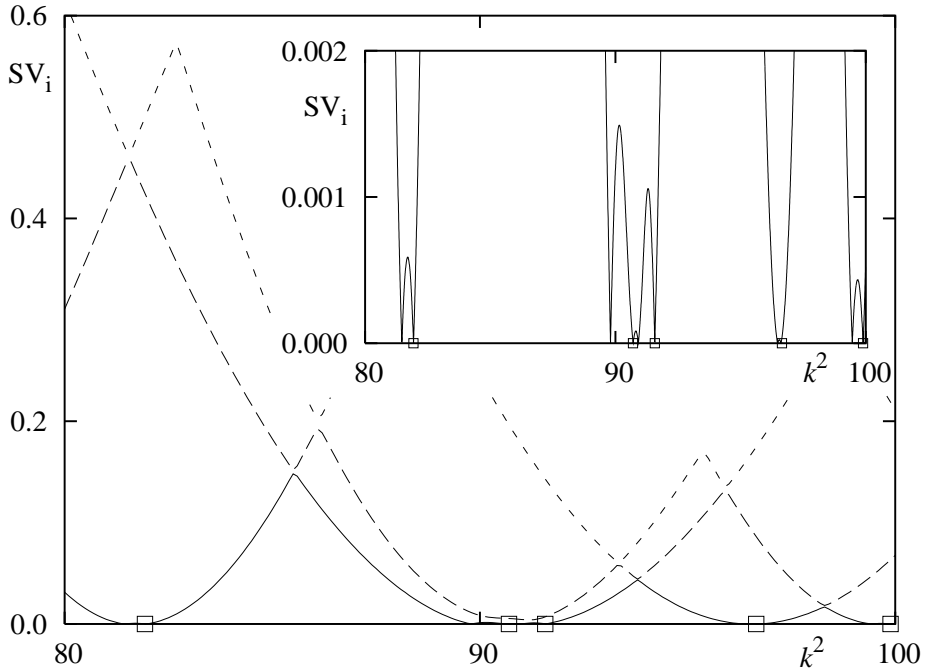


Figure 21: Using the real Green function (82) leads to spurious solutions (see the inset) in addition to the correct eigenvalues marked by squares (compare with fig. 17). For each true solution there is an additional spurious one (hardly visible at $k^2 \approx 91$ and $k^2 \approx 96$).

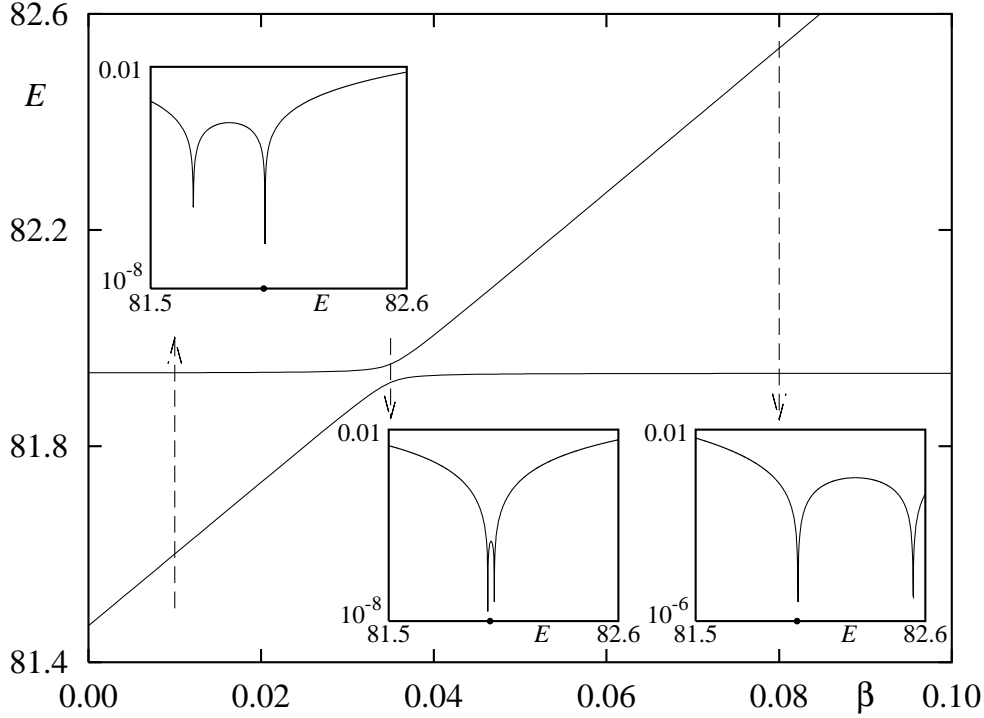


Figure 22: Plot of the minima of the singular values around the eigenvalue $k^2 = 81.93\dots$ with varying β using the parametrized Green function (83). The insets show the corresponding structure of the first singular value with a logarithmic vertical scale (matrix size for this computation: $N = 200$).

lose their nice linear structure, see fig. 21. To overcome the problem of these additional zeros a parametrized Green function

$$G_k^{(\beta)}(\mathbf{q}, \mathbf{q}') = \frac{1}{4} [\beta J_0(k|\mathbf{q} - \mathbf{q}'|) + Y_0(k|\mathbf{q} - \mathbf{q}'|)] \quad (83)$$

is used in [58]. Thus for $\beta = 0$ we obtain eq. (82) and for $\beta = -i$ we get eq. (61). So using a purely real Green function means to vary $\beta \in \mathbb{R}$ which changes the location of the spurious solutions but not those of the true ones. This is illustrated in fig. 22 around the eigenvalue $k^2 = 81.93\dots$ with $\beta \in [0, 0.1]$. Clearly on this scale the true solution does not change under variation of β (apart from the region of the avoided crossing which is due to the finite matrix size and gets smaller for larger N) whereas the spurious solution strongly varies with β . For $\beta = -\gamma i$ with increasing real γ the additional zeros move away from the real axis and it seems that for $\beta = -i$ they do not have any significant influence on the real axis. Still there could be cases where also for $\beta = -i$ such a solution becomes relevant, but for convex geometries we have not encountered this situation. For an example of a non-convex geometry see section 3.3.6.

As an explicit example for the influence of parameterized Green function (83) let us consider the circular billiard with radius 1, where the Fredholm determinant reads (see e.g. [58, 74])

$$D(k) = \prod_{l=-\infty}^{\infty} \left[-i\pi k H_l^{(1)'}(k) J_l(k) \right] . \quad (84)$$

As this product converges absolutely in the whole complex k -plane (apart from a cut along the negative real axis) zeros of $D(k)$ occur when one of the factors in the product vanishes [74]. Clearly, the real zeros of $D(k)$ correspond to the eigenvalues j_{ml} of the circular billiard with radius 1 and Dirichlet boundary conditions. The further zeros stem from the functions $H_l^{(1)'}(z)$ which have only zeros with $\text{Im } z < 0$ [82], and do not correspond to physical solutions of the interior problem. However, they can be related to resonances of the exterior scattering problem, but with Neumann boundary conditions [76, 77]. Because of the radial symmetry the S -matrix is diagonal in angular momentum space

$$S_{l'l} = -\frac{H_l^{(2)'}(k)}{H_l^{(1)'}(k)} \delta_{l'l} \quad (85)$$

and therefore the resonances are at those complex k for which

$$H_l^{(1)'}(k) = 0 \quad , \quad (86)$$

i.e. the same condition as implied by (84).

If one uses the parametrized Green function (83) one can show (analogous to the derivation of eq. (84)) that for the circular billiard

$$D^{(\beta)}(k) = \prod_{l=-\infty}^{\infty} [\pi k (\beta J_l'(k) + Y_l'(k)) J_l(k)] \quad . \quad (87)$$

For $\beta = 0$, which corresponds to the real Green function (82), we get additional zeros of $D^{(0)}(k)$ when $Y_l'(k) = 0$. Varying β from zero to $-i$ these real zeros turn complex. At first sight one might think that these are connected to the places with $H_l^{(1)'}(k) = 0$, however numerical computations show that (for all studied cases) these move away from the real axis with a positive imaginary part and for $\beta = -i$ one has $H_l^{(1)'}(k) = 0$ only for $\text{Im } k < 0$. Thus the spurious solutions for the real Green function are not related to resonances of the scattering problem with Neumann boundary conditions.

These examples suggest to use the full complex Green function (61) instead of the real variant (82). Even though the numerical computation is more time-consuming for the complex case their advantages over choosing (82) are obvious as the variation of β is time-consuming as well (and non-trivial to implement in an automatic way).

3.3.6 Spurious solutions II: Non-convex geometries

Even when choosing the complex Green function (61) it is possible to encounter spurious solutions: For the circular the additional complex zeros of $D(k)$ are sufficiently far away from the real axis, i.e. $\text{Im } k \ll 0$ so that they do not lead to problems with the application of the boundary integral method. However, when one considers different geometries the resonances of the corresponding scattering system could be closer to the real axis. This can be nicely studied for the annular sector billiard, see fig. 23, as the eigenvalues and eigenfunctions can be determined numerically with arbitrary accuracy. Using the ansatz [83, §25]

$$\psi(r, \phi) = [J_\nu(kr) + cY_\nu(kr)] \sin(\nu\phi) \quad (88)$$

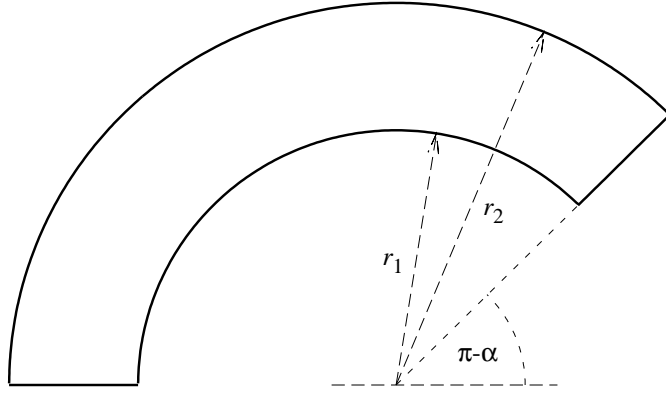


Figure 23: Boundary of the annular sector billiard for $\alpha = \frac{7}{8}\pi$ and $r_1 = 0.4$ and $r_2 = 0.6$.

with $\nu = m\frac{\pi}{\alpha}$, $m = 0, 1, 2, \dots$ and requiring $\psi(r_1, \phi) = 0$ and $\psi(r_2, \phi) = 0$ gives the (implicit) eigenvalue equation

$$J_\nu(kr_1)Y_\nu(kr_2) - Y_\nu(kr_1)J_\nu(kr_2) = 0 . \quad (89)$$

For each m one gets a sequence of zeros $k_{mn} = \sqrt{E_{mn}}$.

Fig. 24 shows for the annular sector billiard with $\alpha = \frac{49}{50}\pi$ the first three singular values as a function of k^2 . The solutions of (89) are marked by triangles. Clearly, there are additional minima, which can be associated with resonances of the dual scattering problem (for further details and examples of this association for the annular sector billiard see [84]). In the limit of $\alpha \rightarrow \pi$ these resonances are given by the eigenvalues of the circular billiard of radius r_1 with Neumann boundary conditions. For this billiard the ansatz $\psi(r, \phi) = J_m(kr)$ together with $\frac{\partial \psi(r, \phi)}{\partial r} \Big|_{r=r_1} = 0$ gives the eigenvalue equation

$$mJ_m(kr_1) - kr_1J_{m+1}(kr_1) = 0 . \quad (90)$$

The circles shown in fig. 24 correspond to the solutions of (90) and provide a very good description of the additional minima.

Thus the question arises how to detect and distinguish these additional solutions. First, of course their existence and relevance strongly depends on the system one is studying. In many situations (for example convex geometries) there appear to be no complex solutions coming close enough to the real axis. Intuitively this seems reasonable as long as there are no trapped orbits outside of the billiard as these should give rise to resonances with small imaginary part.

However, if such additional solutions exist they will show up in the δ_n statistics by an offset of +1 at each additional eigenvalue (unless one by chance misses the same number of ‘correct’ eigenvalues). If one has a system with such additional solutions one approach is to plot the corresponding normal derivative function $u(s)$ and the eigenfunction. Usually they will behave quite differently for a correct eigenvalue and for a spurious solution. For example for the case of the annular sector billiard the normal derivative function for a spurious solution is discontinuous along the boundary and the corresponding eigenfunction also has contributions outside of the billiard,

see fig. 26. Another test would be to use the normalization condition (91) for the normal derivative and compute the norm of the eigenfunction in the interior of the billiard. These two are the same for proper eigenfunctions whereas for spurious solutions they will disagree. Unfortunately, this is a highly inefficient method as the computation of the eigenfunction in Ω is quite time-consuming. Instead of computing the normalization for the full billiard one could restrict to smaller subregions, e.g. for the annular sector billiard one could integrate over the region of the circle with radius r_1 and check if it is different from zero indicating a spurious solution. For the annular sector billiard the additional zeros of the Fredholm determinant $D(k)$ are complex as long as $\alpha < \pi$. Thus for $N \rightarrow \infty$ these minima will stay bounded away from zero in contrast to the minima corresponding to the eigenvalues. However, in practice it is not possible to check this as one has to make N too large to distinguish these from the correct eigenvalues.

More generally, spurious solutions can be understood by a second look at the boundary integral equations. Namely, for the interior Dirichlet problem we have the *single layer* equation, eq. (59), and the *double layer* equation, eq. (65). On the other hand, the single-layer equation for the outside scattering problem with Neumann boundary conditions at $\partial\Omega$ is also given by the double layer equation (65). (see e.g. [51, 50]). As a consequence, scattering solutions of the outside scattering problem with Neumann boundary conditions at $\partial\Omega$ may become relevant for real k . Namely, for resonances with small imaginary part they can lead to additional solutions for the double layer equation which are numerically indistinguishable from the correct solutions. However, these solutions do not correspond to solutions of the interior problem and they do not fulfill the single layer equation. So a possibility to distinguish spurious solutions for the interior Dirichlet problem is to check the validity of the single layer equation as well, which is only fulfilled simultaneously for correct solutions of the interior Dirichlet problem.

A common approach (see e.g. [50] and references therein) to incorporate this from the beginning is by combining the single layer and double layer equation using a linear superposition. By this the solutions of the outside problem with Neumann boundary conditions can be removed. Because of the singular kernel in the single layer equation special care has to be taken with the implementation. For the more difficult case of billiards with magnetic field see [65].

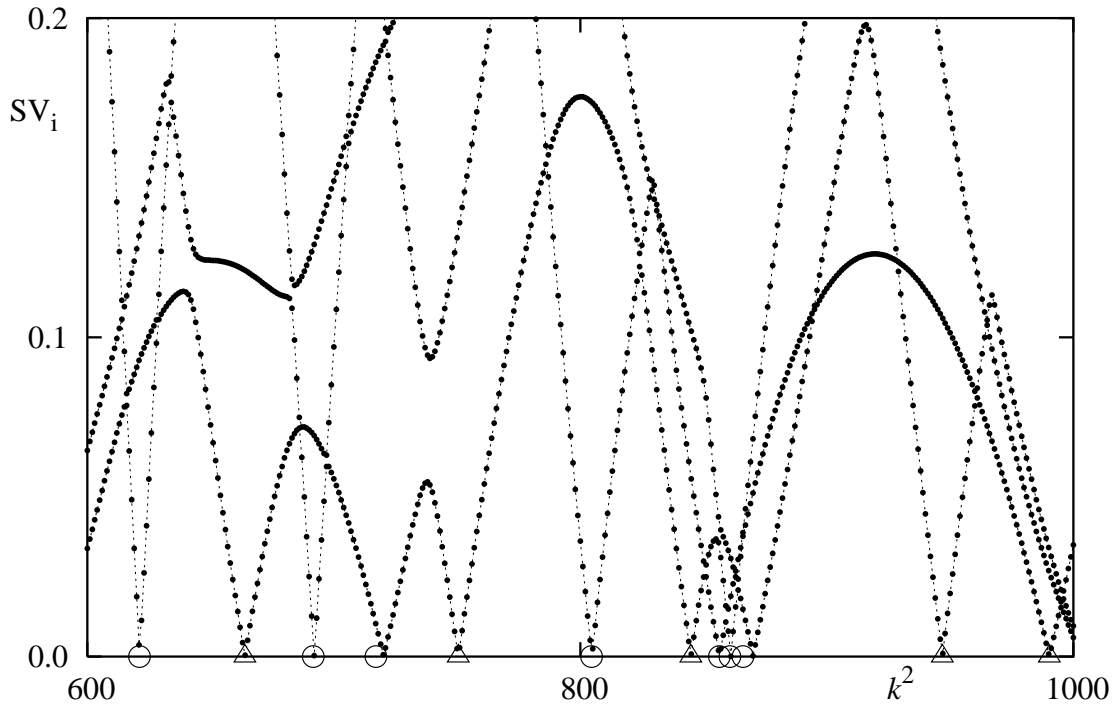


Figure 24: First three singular values as a function of $E = k^2$ of the annular sector billiard for $\alpha = \frac{49}{50}\pi$ and $r_1 = 0.4$ and $r_2 = 0.6$. The triangles correspond to the exact eigenvalues for the annular sector billiard, computed from eq. (89) and the circles correspond to the eigenvalues of the circular billiard with radius r_1 and Neumann boundary condition, determined via eq. (90).

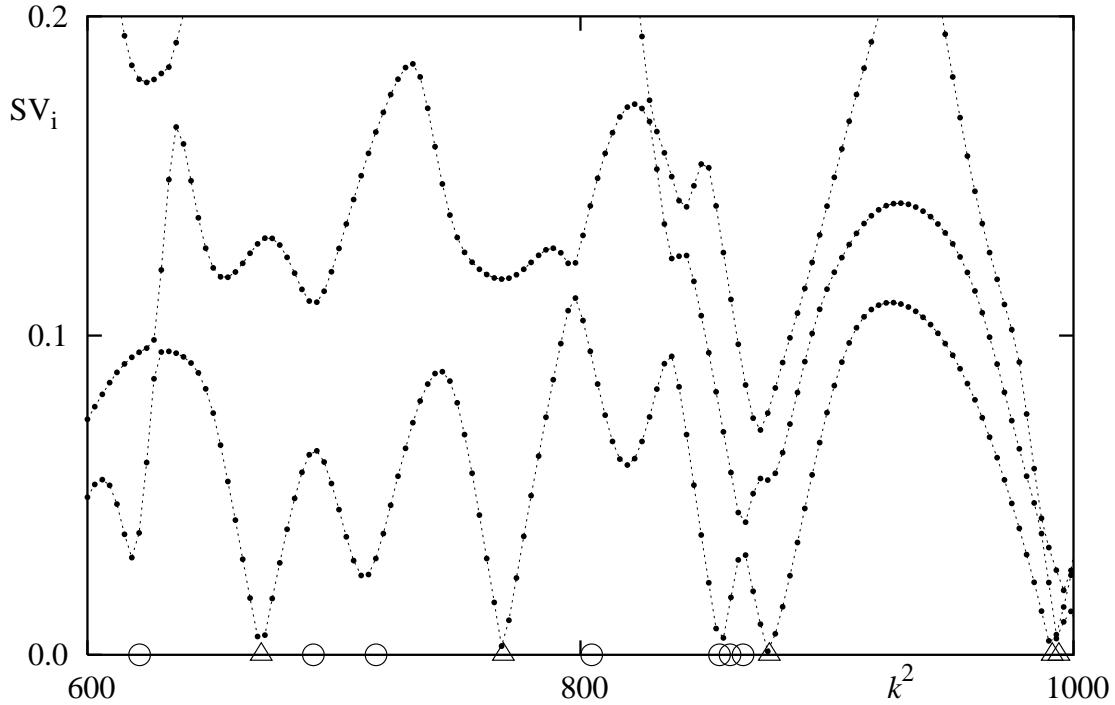


Figure 25: First three singular values as a function of $E = k^2$ of the annular sector billiard for $\alpha = \frac{7}{8}\pi$ and $r_1 = 0.4$ and $r_2 = 0.6$. The triangles correspond to the exact eigenvalues for the annular sector billiard, computed from eq. (89) and the circles correspond to the eigenvalues of the circular billiard with radius r_1 and Neumann boundary condition, determined via eq. (90)

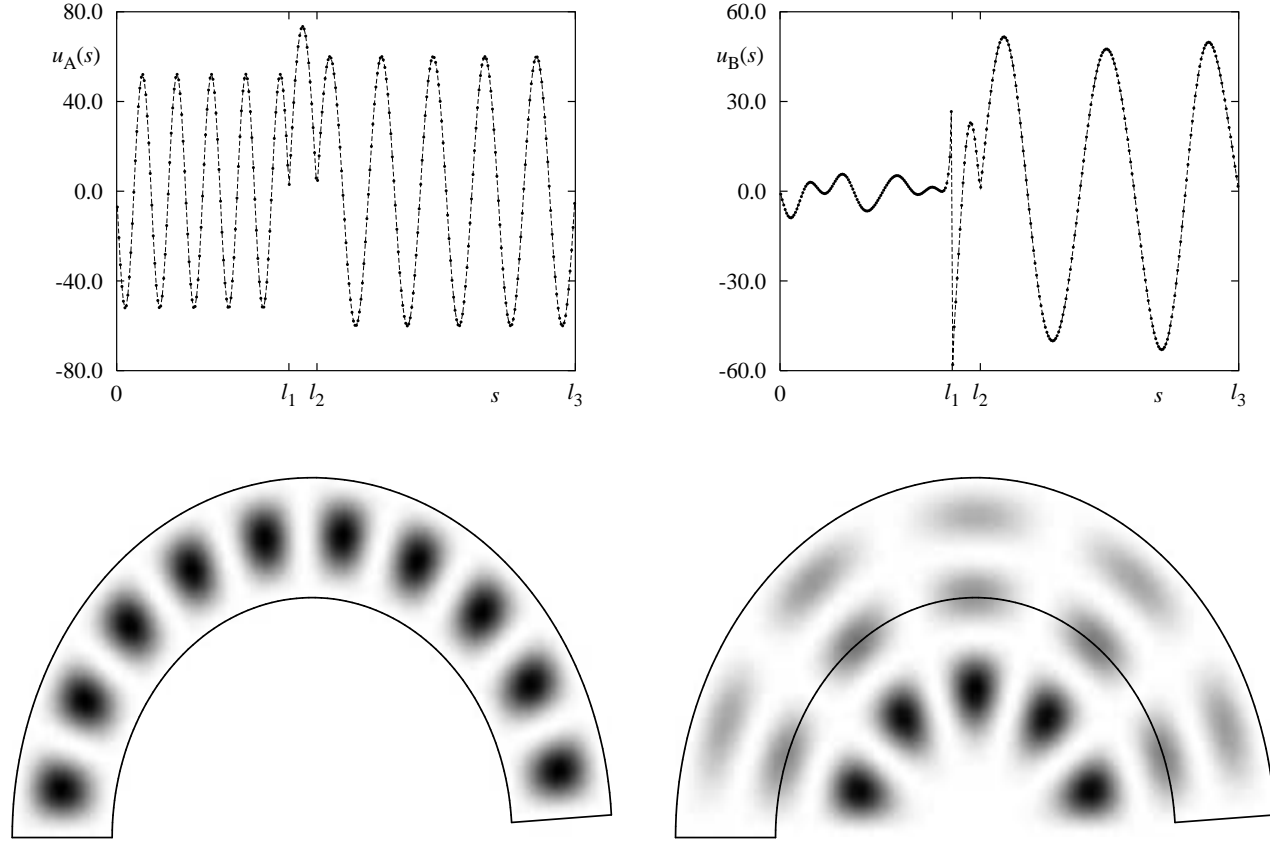


Figure 26: Normal derivative functions $u_n(s)$ corresponding to the correct eigenvalue with $E = 663.88\dots$ (left) and the spurious one with $E = 691.77\dots$ (right). Here $l_1 = r_1\alpha$, $l_2 = r_1\alpha + r_2 - r_1$ and $l_3 = r_1\alpha + r_2 - r_1 + \alpha r_2$. One clearly sees the discontinuity in $u_n(s)$ for the spurious solution. This is also reflected in the structure of the eigenfunction which for the spurious solution has its main contribution outside of the billiard. Notice that in both cases the eigenfunction has been computed according to (80) inside and outside of Ω . The fact that for the correct eigenfunction $\psi_n(\mathbf{q}) = 0$ (within the numerical accuracy) for $\mathbf{q} \in \mathbb{R}^2 \setminus \Omega$ is another test of the accuracy of the eigenvalue computations and eigenfunctions.

3.3.7 Derived quantities in terms of the normal derivative function

As the normal derivative function contains all information to determine the eigenfunction, it is interesting to see if this approach can be used to compute other quantities of interest. For example, if one wants to calculate expectation values $\langle \psi | A | \psi \rangle$ of some operator A in the state ψ , one has to ensure that the eigenfunction ψ is normalized, $\langle \psi | \psi \rangle = \int_{\Omega} |\psi(\mathbf{q})|^2 d^2q = 1$. In principle this could be done by considering $(\langle \tilde{\psi} | \tilde{\psi} \rangle)^{-1} \tilde{\psi}(\mathbf{q})$ of an unnormalized eigenfunction $\tilde{\psi}$. However, an accurate computation of $\langle \tilde{\psi} | \tilde{\psi} \rangle$ using (81) is quite time consuming. Fortunately, there is a simpler way to achieve a normalized ψ : If ψ is a normalized eigenfunction with eigenvalue $E = k^2$ and $u(s)$ is the corresponding normal derivative then we have the following normalization condition

for $u(s)$ [55, 59]

$$\frac{1}{2} \oint_{\partial\Omega} \mathbf{n}(s) \mathbf{q}(s) |u(s)|^2 ds = k^2 . \quad (91)$$

If $\tilde{u}(s)$ is an unnormalized normal derivative, then one obtains by

$$u(s) = \frac{\sqrt{2} k}{\sqrt{\oint_{\partial\Omega} \mathbf{n}(s) \mathbf{q}(s) |\tilde{u}(s)|^2 ds}} \tilde{u}(s) \quad (92)$$

a normalized one. Starting with a normal derivative normalized in this way, any other quantities (e.g. expectation values) determined in terms of $u(s)$ have the correct normalization.

This is just the first example out of many highlighting the importance of the normal derivative for numerical computations of quantities related to eigenfunctions. For example, there are explicit expressions in terms of $u_n(s)$ to compute the

- normalization of ψ , eq. (91), [55, 59]
- eigenfunction ψ , eq. (81)
- momentum distribution

$$\hat{\psi}_n(\mathbf{p}) = \frac{1}{2\pi} \int_{\Omega} e^{-i\mathbf{p}\mathbf{q}} \psi_n(\mathbf{q}) d^2q = -\frac{i}{4\pi p_n^2} \int_{\partial\Omega} e^{-i\mathbf{p}\mathbf{q}(s)} \mathbf{p}\mathbf{q}(s) u_n(s) ds , \quad (93)$$

and radially integrated momentum distribution [85, 86]

$$I(\varphi) := \int_0^\infty \left| \hat{\psi}_n(r, \varphi) \right|^2 r dr , \quad (94)$$

see [86] for details.

- Husimi functions (see e.g. [87, 88])
- autocorrelation function of eigenstates [89].

In figs. 27–29 we show for the cardioid billiard examples of eigenfunctions in position space, the corresponding momentum distributions, the angular momentum distributions (for further details and examples see [86]) and the corresponding Husimi functions $H_n(s, p)$. The first example in fig. 27 shows an example of a scarred state, i.e. an eigenstate which shows localization round an unstable periodic orbit [90]. Below the three-dimensional plot of the state is the corresponding density plot (black corresponding to high intensity) in which the localization is clearly visible. Also the corresponding three-dimensional plot of the momentum distribution $\hat{\psi}_{567}(\mathbf{p})$ reveals enhanced contributions in the directions $\varphi = \pi/2, 3\pi/2$. This is also seen in the plot of $I_{567}(\varphi)$ which shows that the probability to find the particle with momentum near $\pi/2$ is significantly enhanced compared to the mean of $1/(2\pi)$. Another representation is the Husimi–Poincaré representation $H_n(s, p)$ where s corresponds to the arclength coordinate along the billiard boundary and p corresponds to the projection of the unit velocity vector after the reflection on the tangent in the

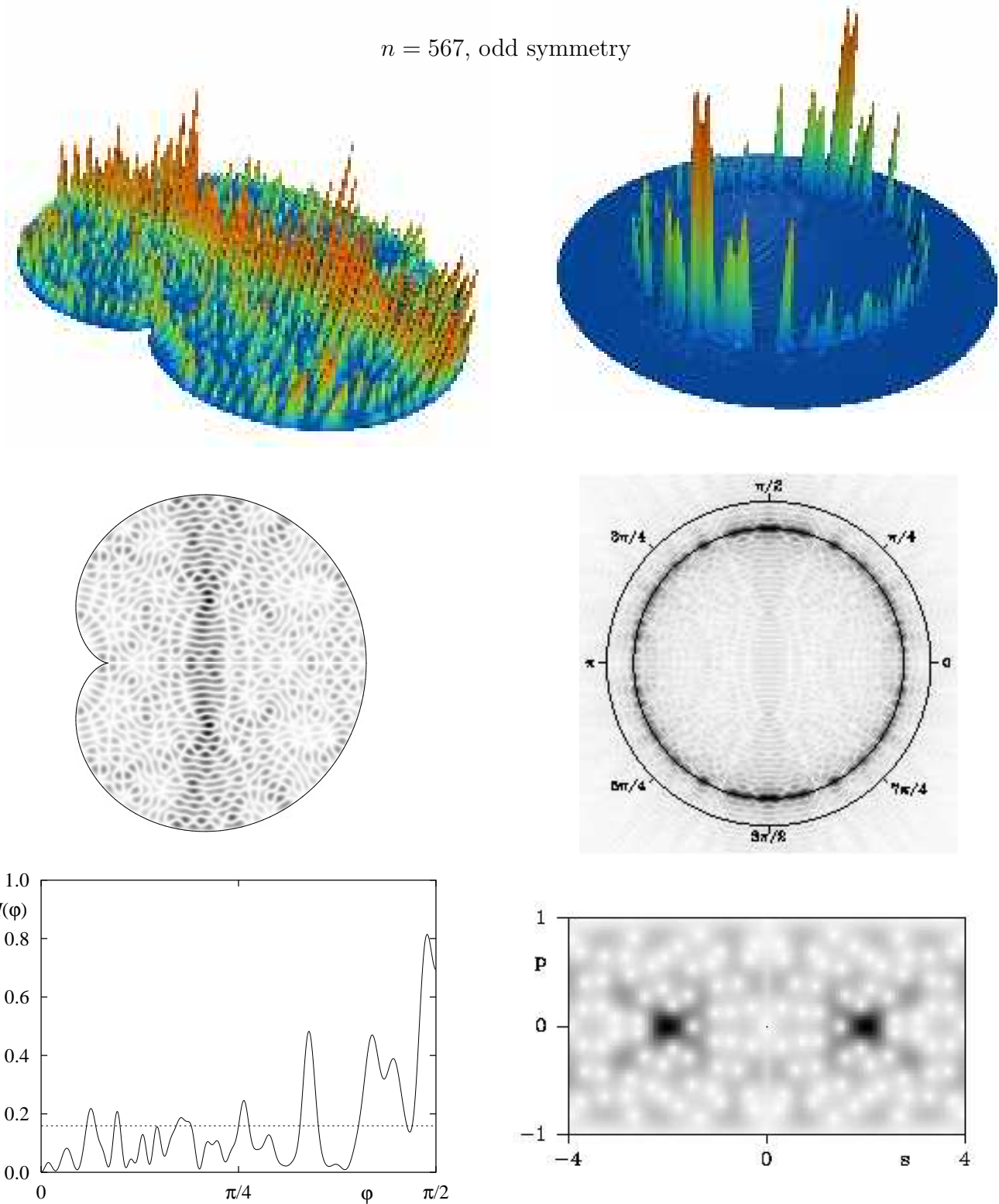


Figure 27: Three-dimensional plots of $|\psi_{567}(\mathbf{q})|^2$, $|\widehat{\psi}_{567}(\mathbf{p})|^2$, their corresponding grey-scale pictures and the plot of the radially integrated momentum distribution $I_{567}(\varphi)$. The momentum distribution $|\widehat{\psi}_{567}(\mathbf{p})|^2$ is concentrated around the energy shell, which is indicated by the inner circle. This state is localized along the shortest unstable periodic orbit, leading to an enhancement of $|\widehat{\psi}_{567}(\mathbf{p})|^2$ near to $\varphi = \pi/2, 3\pi/2$, also seen in the plot of $I_{567}(\varphi)$ near to the momentum direction $\varphi = \pi/2$ (marked by a triangle). This localization is also clearly visible in the Husimi representation.

$n = 116$, odd symmetry

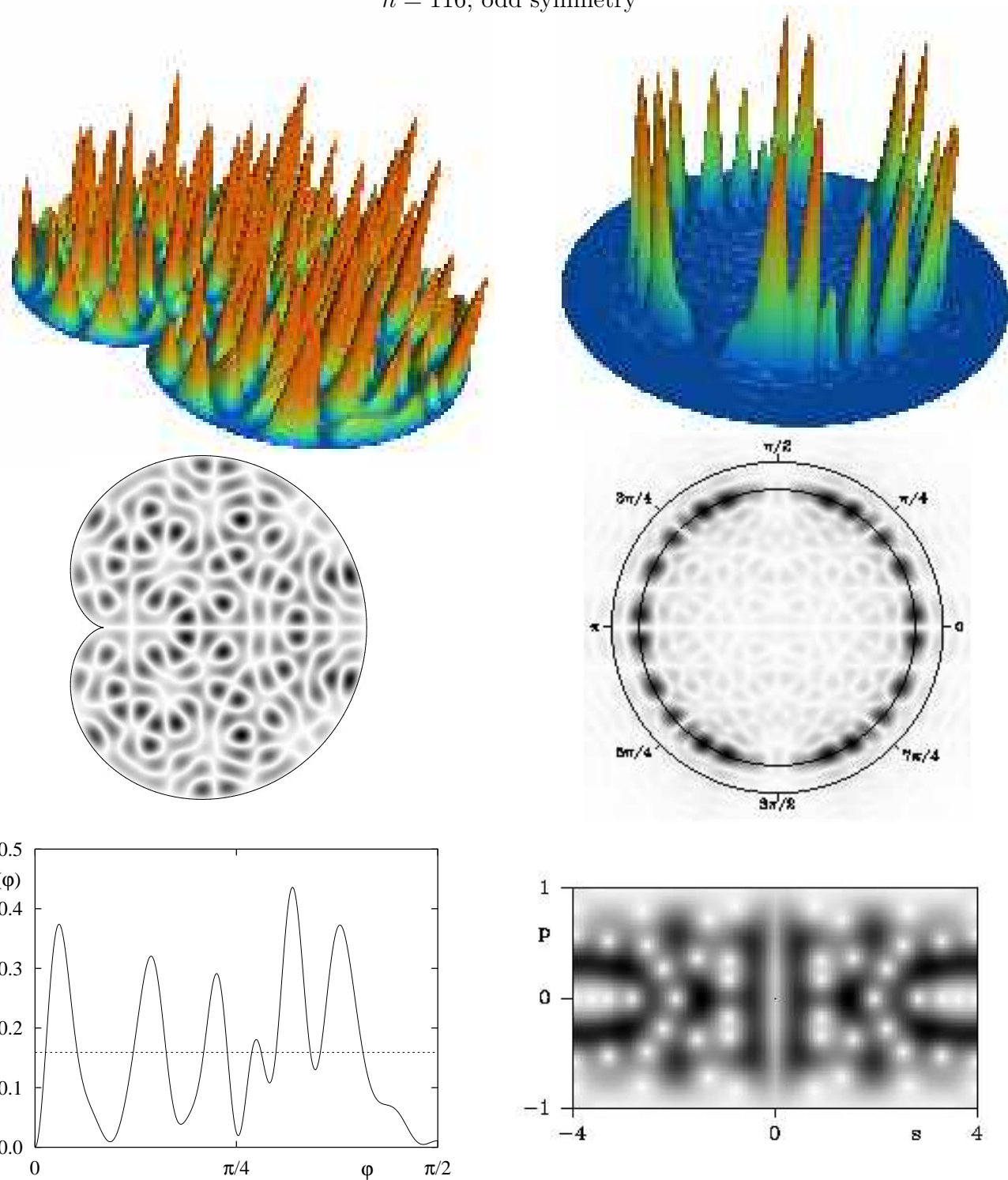


Figure 28: Same as in the previous figure but for $n = 116$. In this case there is no prominent localization neither in position nor in momentum space.

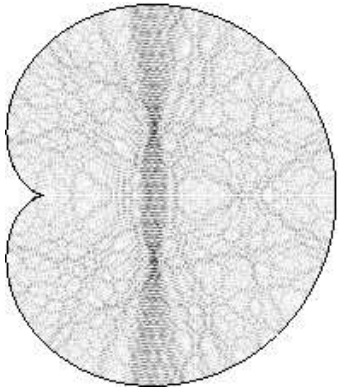
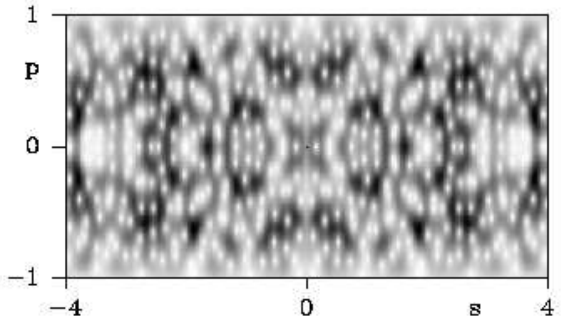
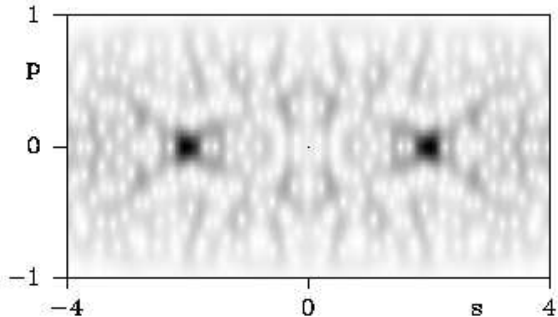
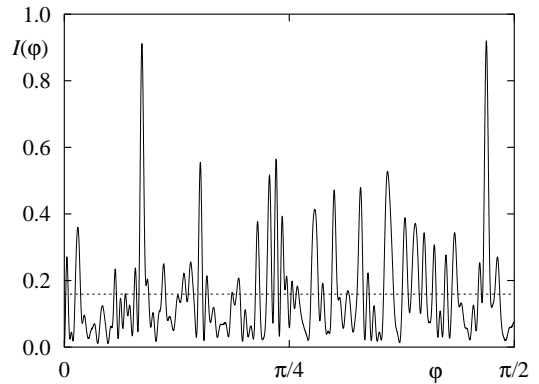
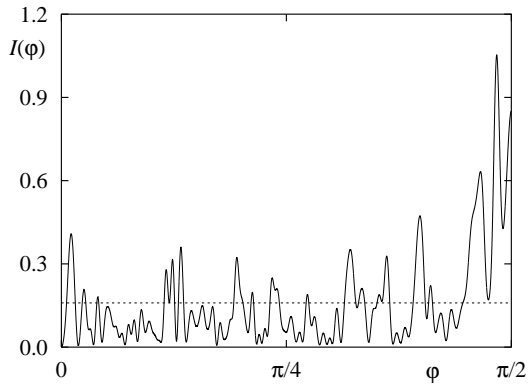
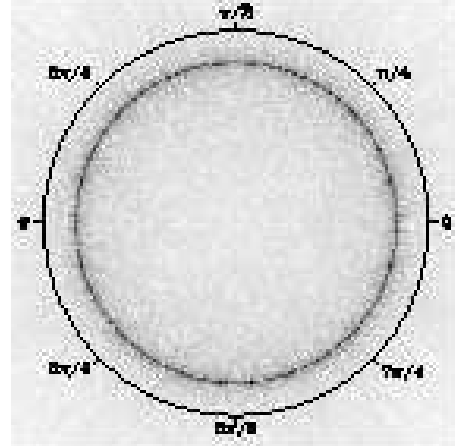
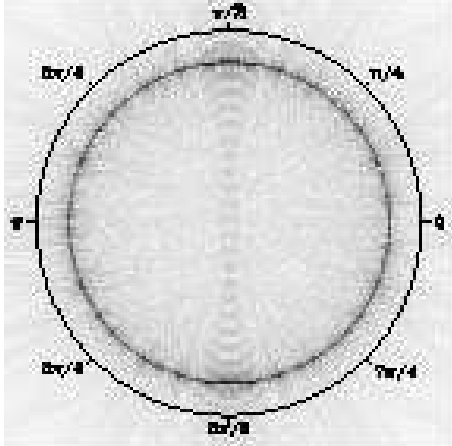
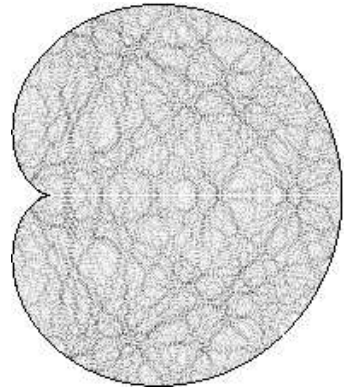
a) $n = 4042$, odd symmetryb) $n = 6000$, odd symmetry

Figure 29: The eigenfunction in a) shows localization along the shortest unstable orbit which is also reflected in the momentum distributions and in the Husimi function. The eigenfunction in b) is an example which appears to be quite delocalized both in position and in momentum space. The pictures look like those expected (according to the quantum ergodicity theorem) for a ‘typical’ eigenfunction.

point s . In this picture the localization around the unstable orbit is maybe most clearly seen; the places of high intensity are on the line $p = 0$ (perpendicular reflection) and match perfectly with the position of the orbit.

The second example shown in fig. 28 is an ‘ergodic’ state, i.e. a state which does not show any significant localization (as much as something like this is possible at low energies) neither in position nor in momentum space (apart from the localization on the energy shell). This is nicely reflected in the various representations. Two further examples are shown in fig. 29 where a) is a higher lying scar and b) is another ‘typical’ state (in the sense of the quantum ergodicity theorem).

4 Concluding remarks — or what's left ?

There are many more issues related to scientific computing in quantum chaos which I did not mention in these notes. They for example include visualization techniques, programming of parallel computers (e.g. using PVM or MPI), or using vector computers etc. Also the more implementation specific aspects, including the choice of a programming language have not been discussed. A good starting point to learn about computing in quantum chaos are quantum maps as their numerics is much easier (one can use a black-box routine to get all eigenvalues at once) than for billiard systems, where more complicated methods have to be used.

Acknowledgements

I would like to thank the organizers of the summer school *The Mathematical aspects of Quantum Chaos I* in Bologna, Mirko Degli Esposti and Sandro Graffi for all their effort, especially Mirko for dealing with everything (including food and wine ;-) in the ‘Italian way’! Moreover, I am grateful to Grischa Haag for many discussions on quantum maps, and Ralf Aurich for discussions on the boundary element method. I would like to thank Professor Frank Steiner and Silke Fürstberger for useful comments on the manuscript and Professors Uzy Smilansky and Andreas Knauf for useful remarks on an earlier version of this text. I would like to thank Fernando Perez for pointing out some speed improvements of the **Python** implementation. Most parts of this work have been done during my stay at the School of Mathematics, University of Bristol, and the Basic Research Institute in the Mathematical Sciences, Hewlett-Packard Laboratories Bristol, UK. In particular I would like to thank Professors Jonathan Keating and Sir Michael Berry for all their support. Moreover, I am particularly indebted to Professor Steiner and the University of Ulm for their support throughout the last months. I acknowledge partial support by the Deutsche Forschungsgemeinschaft under contract No. DFG-Ba 1973/1-1.

Appendix: Computing eigenvalues of quantum maps

The first thing when thinking of solving a certain problem numerically is to decide on the programming language. There are numerous possibilities, ranging from Assembler, Fortran, Pascal, C, C++, Java, etc. to using packages like Octave, Matlab, Maple or Mathematica. Here I will use the quite recent scripting language **Python** [91]. Of course it is beyond the scope of this text to give an introduction to this language; several excellent introductions can be found on the Python homepage. In addition to the basic Python installation you will also need the **Numeric** package [92], which is also simple to install. The following programs together with further information can be obtained from [20]. If you have been wondering about the name – yes it originates

from Monty Python's flying circus, and at several places the documentation refers to more or less famous Monty Python sketches.

So here is `pert_cat.py` (the full version can be obtained via [20]):

```
#!/usr/bin/env python

import cmath
from Numeric import zeros,Float,Complex
from math import sin,pi,sqrt
import LinearAlgebra

def quantum_cat(N,kappa):
    """For a given N and kappa this functions returns the corresponding
    unitary matrix U of the quantized perturbed cat map.
    """
    mat=zeros((N,N), Complex)      # complex matrix with NxN elements
    I=1j                           # predefine sqrt(-1)
    # now fill each matrix element
    # (note: this can be done much faster, see the on-line version)
    for k in range(0,N):
        for l in range(0,N):
            mat[k,l]=cmath.exp(2.0*I*pi/N*(k*k-k*l+l*l)+ \
                I*kappa*N/2.0/pi*sin(2.0*pi/N*l))/sqrt(N)
    return(mat)

def compute_evals_pcat(N,kappa):
    """For a given N and kappa this functions returns the eigenvalues
    and eigenphase of the unitary matrix U filled via quantum_cat(N,kappa).
    """
    matU=quantum_cat(N,kappa)      # fill matrix U_N
    evals=LinearAlgebra.eigenvalues(matU) # determine eigenvalues of U_N

    # determine phase \in [0,2\pi] from the eigenvalues
    phases_N = arctan2(evals.imag,evals.real) + pi
    # useful to determine level-spacing
    phases = concatenate([phases_N,[phases_N[0]+2.0*pi]])
    return(evals,phases)

### Main (used if pert_cat.py is called as script)
if __name__ == '__main__':
    from string import atoi,atof
    import sys

    # Determine eigenvalues and eigenphases
    (evals,phases)=compute_evals_pcat(atoi(sys.argv[1]),atof(sys.argv[2]))

    for k in range(0,N):          # print eigenvalues
        print("% e % e % e % e" % \
            (evals[k].real,evals[k].imag,phases[k],abs(evals[k])))
```

The only drawback of the above code is that the loop to fill the matrix is slower than a corresponding code in C or Fortran (notice that there are some very nice ways of overcoming this by inlining of code or on-the-fly compilation which are presently being developed for example in the context of SciPy [93]). However, as `diagonalize` uses the LAPACK library the most time-consuming part (at least for larger N) is done in an efficient way (not taking into account the possibility of using ATLAS [24] for further speed improvements).

As a first test do (for $N = 101$ and $\kappa = 0.3$)

```
python pert_cat.py 101 0.3
```

It will output the (complex) eigenvalues as a sequence x, y pairs. As a test, whether these all lie on the unit circle the third column is the absolute value of the eigenvectors. To plot the resulting data you may use

```
python pert_cat.py 101 0.3 > pcat_101_0.3.dat
```

which redirects the output of the program to the file `pcat_101_0.3.dat`. To plot the resulting file use your favourite plotting program, e.g. for `gnuplot` [94] just do

```
plot "pcat_101_0.3.dat" using 1:2 with points
```

Now we would like to compute the level spacing distribution. To do this let us use an interactive Python session in which we do

```
from Numeric import *                      # Numeric package
from pert_cat import compute_evals_pcat  # the above pert_cat routines
from AnalyseData import *                  # histogram routine (see below)

N=53
kappa=0.3
(evals,phases)=pert_cat.compute_evals_pcat(N,kappa);
# sort and unfold phases
s_phases=Numeric.sort(phases)*N/(2.0*pi)

# determine Level spacing
# (by computing the difference of the shifted eigenphases)
spacings=s_phases[1:]-s_phases[0:N]

(x_histogram,y_histogram)=histogram(spacings,0.0,10.0,100)
store_histogram(x_histogram,y_histogram,"histogram.dat")
```

Then use your favourite plotting program to plot the level spacing distribution. For `gnuplot` you could do

```
goe_approx(x)=pi/2.0*x*exp(-pi/4*x*x)
gue_approx(x)=32/pi/pi*x*x*exp(-4/pi*x*x)
plot "histogram.dat" w 1,goe_approx(x),gue_approx(x),exp(-x)
```

Here the routines to compute and store the histogram are in `AnalyseData.py` whose core reads

```

def histogram(data,min,max,nbins):
    from Numeric import *
    # first select only those which lie in the interval [min,max]
    hdat=compress( ((data<max)*(data>min)),data)
    bin_width=(max-min)/nbins
    # define the bins
    bins=min+bin_width*arange(nbins)
    # determine indices
    inds=searchsorted(sort(hdat),bins)
    inds=concatenate([inds,[len(hdat)]])
    # return bins and normalized histogram
    return(bins,(inds[1:]-inds[:-1])/(bin_width*len(hdat)))

def store_histogram(x_distrib,y_distrib,outdat):
    bin_width=x_distrib[1]-x_distrib[0]
    f=open(outdat,"w")                      # open file for writing
    for k in range(0,len(x_distrib)):
        f.write("% e % e \n" % (x_distrib[k],y_distrib[k]))
        f.write("% e % e \n" % (x_distrib[k]+bin_width,y_distrib[k]))
    f.close()

```

Again, for further details and full routines see [20].

References

- [1] J. Meiss: *Symplectic maps, variational principles, and transport*, Rev. Mod. Phys. **64** (1992) 795–848.
- [2] J.-M. Strelcyn: *The “coexistence problem” for conservative dynamical systems: a review*, Colloquium mathematicum **62** (1991) 331–345.
- [3] P. Duarte: *Plenty of elliptic islands for the standard family of area preserving maps*, Ann. Inst. H. Poincaré Anal. Non Linéaire **11** (1994) 359–409.
- [4] A. Giorgilli and V. F. Lazutkin: *Some remarks on the problem of ergodicity of the standard map*, Phys. Lett. A **272** (2000) 359–367.
- [5] V. F. Lazutkin: *A remark on “Some remarks on the problem of ergodicity of the standard map”*, preprint, mp-arc 00-159 (2000).
- [6] M. Basilio de Matos and A. M. Ozorio de Almeida: *Quantization of Anosov maps*, Annals of Physics **237** (1993) 46–65.
- [7] P. A. Boasman and J. P. Keating: *Semiclassical asymptotics of perturbed cat maps*, Proc. R. Soc. London Ser. A **449** (1995) 629–653.
- [8] V. I. Arnold and A. Avez: *Ergodic Problems of Classical Mechanics*, Benjamin, New York, (1968).
- [9] M. V. Berry, N. L. Balazs, M. Tabor and A. Voros: *Quantum maps*, Annals of Physics **122** (1979) 26–63.
- [10] J. H. Hannay and M. V. Berry: *Quantization of linear maps on a torus — Fresnel diffraction by periodic grating*, Physica D **1** (1980) 267–290.

- [11] N. L. Balazs and A. Voros: *The quantized Baker's transformation*, Ann. Phys. **190** (1989) 1–31.
- [12] M. Saraceno: *Classical structures in the quantized baker transformation*, Ann. Phys. **199** (1990) 37–60.
- [13] M. Degli Esposti: *Quantization of the orientation preserving automorphisms of the torus*, Ann. Inst. H. Poincaré Phys. Théor. **58** (1993) 3 323–341.
- [14] M. Degli Esposti, S. Graffi and S. Isola: *Classical limit of the quantized hyperbolic toral automorphisms*, Commun. Math. Phys. **167** (1995) 471–507.
- [15] S. De Bièvre, M. Degli Esposti and R. Giachetti: *Quantization of a class of piecewise affine transformations on the torus.*, Commun. Math. Phys. **176** (1996) 73–94.
- [16] S. Zelditch: *Index and dynamics of quantized contact transformations.*, Ann. Inst. Fourier **47** (1997) 305–363.
- [17] G. Haag: *Quantisierte chaotische Abbildungen*, Diploma Thesis, Abteilung Theoretische Physik, Universität Ulm (1999).
- [18] S. De Bièvre: *Quantum chaos: a brief first visit* in: *Second Summer School in Analysis and Mathematical Physics: Topics in Analysis: Harmonic, Complex, Nonlinear and Quantization*, S. Perez-Esteva and C. Villegas-Blas (eds.), Contemporary Mathematics **289** (2001).
- [19] T. Prosen and M. Robnik: *Numerical demonstration of the Berry-Robnik level spacing distribution*, J. Phys. A **27** (1994) L459–L466, corrigendum: ibid. **27** (1994) 6633–6633.
- [20] See <http://www.physik.uni-ulm.de/theo/qc/baec/qmaps.html> for programs and further information.
- [21] The Numerical Algorithms Group (NAG), <http://www.nag.co.uk/>.
- [22] LAPACK – Linear Algebra PACKage, <http://www.netlib.org/lapack/>.
- [23] R. Ketzmerick, K. Kruse and T. Geisel: *Efficient diagonalization of kicked quantum systems*, Physica D **131** (1999) 247–253.
- [24] ATLAS, <http://math-atlas.sourceforge.net/> (Automatically Tuned Linear Algebra Software).
- [25] O. Bohigas, M.-J. Giannoni and C. Schmit: *Characterization of chaotic quantum spectra and universality of level fluctuation laws*, Phys. Rev. Lett. **52** (1984) 1–4.
- [26] M. V. Berry and M. Tabor: *Level clustering in the regular spectrum*, Proc. R. Soc. London Ser. A **356** (1977) 375–394.
- [27] J. P. Keating: *Asymptotic properties of the periodic orbits of the cat maps*, Nonlinearity **4** (1991) 277–307.
- [28] J. P. Keating: *The cat maps: Quantum mechanics and classical motion*, Nonlinearity **4** (1991) 309–341.
- [29] F. Mezzadri: *Boundary conditions for torus maps and spectral statistics*, Ph.D. thesis, School of Mathematics, University of Bristol, (1999).
- [30] J. P. Keating and F. Mezzadri: *Pseudo-symmetries of Anosov maps and spectral statistics*, Nonlinearity **13** (2000) 747–775.
- [31] T. A. Brody, J. Flores, J. B. French, P. A. Mello, A. Pandey and S. S. M. Wong: *Random-matrix physics: spectrum and strength fluctuations*, Rev. Mod. Phys. **53** (1981) 385–479.
- [32] F. Haake: *Quantum Signatures of Chaos*, Springer-Verlag, Berlin, 2nd edn., (2001).

[33] C. E. Porter and R. G. Thomas: *Fluctuations of Nuclear Reaction Widths*, Phys. Rev. **104** (1956) 483–491.

[34] P. Kurlberg and Z. Rudnick: *Value distribution for eigenfunctions of desymmetrized quantum maps*, Internat. Math. Res. Notices (2001) 995–1002.

[35] B. Eckhardt: *Exact eigenfunctions for a quantised map*, J. Phys. A **19** (1986) 10 1823–1831.

[36] A. Bouzouina and S. De Biévre: *Equipartition of the eigenfunctions of quantized ergodic maps on the torus*, Commun. Math. Phys. **178** (1996) 83–105.

[37] S. De Bièvre and M. Degli Esposti: *Egorov theorems and equidistribution of eigenfunctions for the quantized sawtooth and baker maps*, Ann. Inst. Henri Poincaré, Physique Théorique **69** (1996) 1–30.

[38] A. Bäcker and H. R. Dullin: *Symbolic dynamics and periodic orbits for the cardioid billiard*, J. Phys. A **30** (1997) 1991–2020.

[39] H. P. Baltes and E. R. Hilf: *Spectra of Finite Systems*, Bibliographisches Institut, Mannheim, Wien, Zürich, (1976).

[40] M. Sieber, U. Smilansky, S. C. Creagh and R. G. Littlejohn: *Non-generic spectral statistics in the quantized stadium billiard*, J. Phys. A **26** (1993) 6217–6230.

[41] A. Bäcker, F. Steiner and P. Stifter: *Spectral statistics in the quantized cardioid billiard*, Phys. Rev. E **52** (1995) 2463–2472.

[42] A. Bäcker and F. Steiner: *Quantum chaos and quantum ergodicity*, in: *Ergodic Theory, Analysis and Efficient Simulation of Dynamical Systems*, B. Fiedler (ed.), 717–752, Springer-Verlag Berlin/Heidelberg (2001).

[43] J. R. Kuttler and V. G. Sigillito: *Eigenvalues of the Laplacian in two dimensions*, SIAM Review **26** (1984) 163–193.

[44] E. J. Heller: *Wavepacket dynamics and quantum chaology*, in: *Proceedings of the 1989 Les Houches School on Chaos and Quantum Physics* (Eds. M.-J. Giannoni, A. Voros and J. Zinn Justin), North-Holland, Amsterdam, (1991).

[45] B. Li and M. Robnik: *Statistical properties of high-lying chaotic eigenstates*, J. Phys. A **27** (1994) 5509–5523.

[46] E. Doron and U. Smilansky: *Chaotic Spectroscopy*, Chaos **2** (1992) 117–124.

[47] B. Dietz and U. Smilansky: *A scattering approach to the quantization of billiards – The inside-outside duality*, Chaos **3** (1993) 581–590.

[48] H. Schanz and U. Smilansky: *Quantization of Sinai’s billiard – a scattering approach*, Chaos, Solitons and Fractals **5** (1995) 1289–1309.

[49] E. Vergini and M. Saraceno: *Calculation of highly excited states of billiards*, Phys. Rev. E **52** (1995) 2204–2207.

[50] A. J. Burton and G. F. Miller: *The application of integral equation methods to the numerical solution of some exterior boundary-value problems*, Proc. R. Soc. London Ser. A **323** (1971) 201–210.

[51] R. E. Kleinman and G. F. Roach: *Boundary integral equations for the three dimensional Helmholtz equation*, SIAM Rev. **16** (1974) 214–236.

[52] R. J. Riddel Jr.: *Boundary-distribution solution of the Helmholtz equation for a region with corners*, J. Comp. Phys. **31** (1979) 21–41.

[53] R. J. Riddel Jr.: *Numerical solution of the Helmholtz equation for two-dimensional polygonal regions*, J. Comp. Phys. **31** (1979) 42–59.

[54] P. A. Martin: *Acoustic scattering and radiation problems and the null-field method*, Wave Motion (1982) 391–408.

[55] M. V. Berry and M. Wilkinson: *Diabolical points in the spectra of triangles*, Proc. R. Soc. London Ser. A **392** (1984) 15–43.

[56] M. Sieber and F. Steiner: *Quantum chaos in the hyperbola billiard*, Phys. Lett. A **148** (1990) 415–419.

[57] D. Biswas and S. Jain: *Quantum description of a pseudointegrable system: the $\pi/3$ -rhombus billiard*, Phys. Rev. A **42** (1990) 3170–3185.

[58] P. A. Boasman: *Semiclassical Accuracy for Billiards*, Ph.D. thesis, H. H. Wills Physics Laboratory, Bristol, (1992).

[59] P. A. Boasman: *Semiclassical accuracy for billiards*, Nonlinearity **7** (1994) 485–537.

[60] R. Aurich and F. Steiner: *Statistical properties of highly excited quantum eigenstates of a strongly chaotic system*, Physica D **64** (1993) 185–214.

[61] C. Pisani: *Exploring periodic orbit expansions and renormalisation with the quantum triangular billiard*, Ann. Physics **251** (1996) 208–265.

[62] I. Kosztin and K. Schulten: *Boundary integral method for stationary states of two-dimensional quantum systems*, Int. J. Mod. Phys. C **8** (1997) 293–325.

[63] B. Li, M. Robnik and B. Hu: *Relevance of chaos in numerical solutions of quantum billiards*, Phys. Rev. E **57** (1998) 4095–4105.

[64] M. Sieber: *Billiard systems in three dimensions: the boundary integral equation and the trace formula*, Nonlinearity **11** (1998) 6 1607–1623.

[65] K. Hornberger and U. Smilansky: *The boundary integral method for magnetic billiards*, J. Phys. A **33** (1999) 2829–2855.

[66] R. Aurich and J. Marklof: *Trace formulae for three-dimensional hyperbolic lattices and application to a strongly chaotic tetrahedral billiard*, Physica D **92** (1996) 101–129.

[67] H. Primack and U. Smilansky: *Quantization of the 3-dimensional Sinai billiard*, Phys. Rev. Lett. **74** (1995) 4831–4834.

[68] G. Steil: *Eigenvalues of the Laplacian for Bianchi groups*, in: *Emerging applications of number theory (Minneapolis, MN, 1996)*, 617–641, Springer, New York, (1999).

[69] T. Prosen: *Quantization of generic chaotic 3D billiard with smooth boundary I: energy level statistic*, Phys. Lett. A **233** (1997) 323–331.

[70] T. Prosen: *Quantization of generic chaotic 3D billiard with smooth boundary II: structure of high-lying eigenstates*, Phys. Lett. A **233** (1997) 332–342.

[71] R. D. Ciskowski and C. Brebbia, eds.: *Boundary Element Methods in Acoustics*. Computational Mechanics Publications and Elsevier Applied Science, (1991).

[72] E. B. Bogomolny: *Semiclassical quantization of multidimensional systems*, Nonlinearity **5** (1992) 805–866.

[73] T. Harayama and A. Shudo: *Zeta function derived from the boundary element method*, Phys. Lett. A **165** (1992) 417–426.

[74] B. Burmeister: *Korrekturen zur Gutzwillerschen Spurformel für Quantenbillards*, Diploma Thesis , II. Institut für Theoretische Physik, Universität Hamburg (1995).

[75] M. Sieber, N. Pavloff and C. Schmit: *Uniform approximation for diffractive contributions to the trace formula in billiard systems*, Phys. Rev. E **55** (1997) 2279–2299.

[76] B. Burmeister and F. Steiner: *Exact trace formula for quantum billiards*, unpublished (1995).

[77] S. Tasaki, T. Harayama and A. Shudo: *Interior Dirichlet eigenvalue problem, exterior Neumann scattering problem, and boundary element method for quantum billiards*, Phys. Rev. E **56** (1997) R13–R16.

[78] J.-P. Eckmann and C.-A. Pillet: *Zeta functions with Dirichlet and Neumann boundary conditions for exterior domains*, Helv. Phys. Acta **70** (1997) 44–65.

[79] R. Aurich: private communication.

[80] M. Robnik: *Quantising a generic family of billiards with analytic boundaries*, J. Phys. A **17** (1984) 1049–1074.

[81] T. Prosen and M. Robnik: *Energy level statistics and localization in sparsed banded random matrix ensembles*, J. Phys. A **26** (1993) 1105–1114.

[82] M. Abramowitz and I. A. Stegun (eds.): *Pocketbook of Mathematical Functions*, Verlag Harri Deutsch, Thun – Frankfurt/Main, abridged edn., (1984).

[83] A. Sommerfeld: *Vorlesungen über Theoretische Physik, Band VI: Partielle Differentialgleichungen der Physik*, Harri Deutsch, Thun, (1984).

[84] T. Hesse: *Semiklassische Untersuchung zwei- und dreidimensionaler Billardsysteme*, Ph.D. thesis, Abteilung Theoretische Physik, Universität Ulm, (1997).

[85] K. Życzkowski: *Classical and quantum billiards, integrable, nonintegrable, and pseudo-integrable*, Acta Physica Polonica B **23** (1992) 245–270.

[86] A. Bäcker and R. Schubert: *Chaotic eigenfunctions in momentum space*, J. Phys. A **32** (1999) 4795–4815.

[87] J. M. Tualle and A. Voros: *Normal modes of billiards portrayed in the stellar (or nodal) representation*, Chaos, Solitons and Fractals **5** (1995) 1085–1102.

[88] F. P. Simonotti, E. Vergini and M. Saraceno: *Quantitative study of scars in the boundary section of the stadium billiard*, Phys. Rev. E **56** (1997) 3859–3867.

[89] A. Bäcker and R. Schubert: *Autocorrelation function of eigenstates in chaotic and mixed systems*, J. Phys. A **35** (2002) 539–564.

[90] E. J. Heller: *Bound-state eigenfunctions of classically chaotic Hamiltonian systems: Scars of periodic orbits*, Phys. Rev. Lett. **53** (1984) 1515–1518.

[91] Python, <http://www.python.org/>.

[92] Numerical Python (NumPy), <http://sourceforge.net/projects/numpy/>.

[93] SciPy, <http://www.scipy.org/>.

[94] Gnuplot, <http://www.gnuplot.info/>.